

A PSEUDO-REVERSIBLE NORMALIZING FLOW FOR STOCHASTIC DYNAMICAL SYSTEMS WITH VARIOUS INITIAL DISTRIBUTIONS

M. YANG*, P. WANG†, D. DEL-CASTILLO-NEGRETE*, Y. CAO†, AND G. ZHANG‡

Abstract. We present a pseudo-reversible normalizing flow method for efficiently generating samples of the state of a stochastic differential equation (SDE) with different initial distributions. The primary objective is to construct an accurate and efficient sampler that can be used as a surrogate model for computationally expensive numerical integration of SDE, such as those employed in particle simulation. After training, the normalizing flow model can directly generate samples of the SDE's final state without simulating trajectories. Existing normalizing flows for SDEs depend on the initial distribution, meaning the model needs to be re-trained when the initial distribution changes. The main novelty of our normalizing flow model is that it can learn the conditional distribution of the state, i.e., the distribution of the final state conditional on any initial state, such that the model only needs to be trained once and the trained model can be used to handle various initial distributions. This feature can provide a significant computational saving in studies of how the final state varies with the initial distribution. We provide a rigorous convergence analysis of the pseudo-reversible normalizing flow model to the target probability density function in the Kullback–Leibler divergence metric. Numerical experiments are provided to demonstrate the effectiveness of the proposed normalizing flow model.

Key word. Stochastic differential equations, Normalizing Flows, Fokker-Planck equation

MSC codes. 68Q25, 68R10, 68U05

1. Introduction. The numerical solution of stochastic differential equations (SDE) for large ensembles of initial conditions is at the heart of modeling and simulation in science and engineering. For example, computations of interest to plasma physics rely on the solution of SDE tracking the evolution of electrons and ions in which the deterministic (drift) part describes the interaction with prescribed or self-consistent electromagnetic fields, and the stochastic part describes collisional effects. In fluid mechanics, SDE describe the evolution of passive tracers, e.g. pollutants in the oceans and the atmosphere, advected by prescribed velocity fields under the effect of molecular and/or turbulent diffusion. Further applications of SDE include the simulation of biological and chemical systems. From a mathematical perspective, SDE naturally appear as the discrete particle description formally equivalent to the Fokker-Planck description of the particle distribution function in the continuum limit. This equivalence is the foundation of particle-based Monte-Carlo methods for the numerical solution of Fokker-Planck type partial differential equations (PDE). Although particle based numerical methods offer advantages over continuum methods (e.g., finite difference, fine elements, or spectral), they also face limitations. In particular, to avoid numerical noise, Monte Carlo methods need to integrate SDE for very large ensembles of particles to overcome the unfavorable slow convergence $\sim 1/\sqrt{N}$ where N is the number of initial conditions.

To overcome numerical challenges faced by particle methods, in this paper we propose an efficient and accurate algorithm for the solution of SDE. Our approach is

*Fusion Energy Division, Oak Ridge National Laboratory, Oak Ridge, TN (yangm@ornl.gov, delcastillod@ornl.gov).

†Department of Mathematics, Auburn University, Auburn, AL (pzw0030@auburn.edu, yzc0009@auburn.edu).

‡Computer Science and Mathematics Division, Oak Ridge National Laboratory, Oak Ridge, TN (zhangg@ornl.gov).

based on the use of pseudo-reversible normalizing flows (PR-NF) to efficiently generate samples of the state of an SDE for various initial distributions. Normalizing flows [12, 19, 3, 16, 5, 8, 9] are a class of models that map an unknown probability distribution to a standard probability distribution, e.g., the normal Gaussian distribution, such that one can generate samples from the unknown distribution by sampling the standard distribution and then propagating through the flow model. Normalizing flows have been extended to learn stochastic dynamical systems [1, 13, 7]. However, these models are not transferable, meaning they require model re-training every time the initial distribution is changed.

We improve the normalizing flow models from three perspectives. First, we incorporate the initial state of the SDE as an input variable of the normalizing flow model, so that our method aims at learning the conditional distribution of the state at a given time instant. In this way, a single normalizing flow model can be used to handle different initial distributions by a simple convolution. In this sense, the proposed method can be viewed as an approach to learn the Green's function of the Fokker-Planck equation associated with the SDE. Second, we utilize the pseudo-reversible neural network architecture [10, 24, 20] to relax the strict reversibility constraint. This architecture provides greater flexibility in designing flow transformations and offers potential benefits in terms of performance and applicability. The pseudo-reversible neural network architecture allows to use simple feed-forward neural networks to model both the forward and inverse flows, where an extra loss term is used to ensure pseudo-reversibility. Even though the proposed PR-NF has $\mathcal{O}(d^3)$ complexity in Jacobian determinant computation, we observe that it is not a bottleneck, especially with GPU-accelerated linear algebra libraries, for a wide range of physical processes defined in the six-dimensional phase space. Third, we provide a convergence analysis of the PR-NF model to the target probability density function in the Kullback–Leibler divergence metric, where the simple structure of the PR-NF model makes it feasible to exploit the universal approximation theorem of fully-connected neural networks in our convergence analysis.

The outline of the rest of the paper is as follows. In Section 2 we formulate the problem and define the SDE of interest. The details of the surrogate model based on Normalizing Flows architecture are described in Section 3. Section 4 provides the convergence analysis of the PR-NF model. Section 5 is devoted to examples including a Brownian motion validation model, a problem of interest to magnetically confined fusion plasmas and an advection-diffusion transport problem in fluid mechanics.

2. Problem setting. We consider the d -dimensional stochastic process X_t , corresponding to the solution of the stochastic differential equation

$$(2.1) \quad X_t = X_0 + \int_0^t \mathbf{b}(s, X_s) ds + \int_0^t \boldsymbol{\sigma}(s, X_s) dW_s \quad \text{with } X_0 \in \mathcal{D}, t \in [0, T],$$

where $T > 0$, \mathcal{D} is a bounded domain in \mathbb{R}^d , $\mathbf{b} : [0, T] \times \mathbb{R}^d \rightarrow \mathbb{R}^d$, $\boldsymbol{\sigma} : [0, T] \times \mathbb{R}^d \rightarrow \mathbb{R}^{d \times m}$ are drift and diffusion coefficients, respectively, and $W_s := (W_s^1, \dots, W_s^m)^\top$ is a m -dimensional standard Brownian motion. We assume that \mathbf{b} and $\boldsymbol{\sigma}$ satisfy, for some constant C ,

$$(2.2) \quad |\mathbf{b}(t, \mathbf{x})| + |\boldsymbol{\sigma}(t, \mathbf{x})| \leq C(1 + |\mathbf{x}|), \quad \text{for } \mathbf{x} \in \mathbb{R}^d, t \in [0, T],$$

and

$$(2.3) \quad |\mathbf{b}(t, \mathbf{x}) - \mathbf{b}(t, \mathbf{y})| + |\boldsymbol{\sigma}(t, \mathbf{x}) - \boldsymbol{\sigma}(t, \mathbf{y})| \leq C|\mathbf{x} - \mathbf{y}|, \quad \text{for } \mathbf{x}, \mathbf{y} \in \mathbb{R}^d, t \in [0, T].$$

For an initial state $X_0 \in \mathcal{D}$, the SDE in Eq. (2.1) has a unique time continuous solution X_t [14]. As the state X_t in Eq. (2.1) depends on the initial condition X_0 , we will write X_t in the conditional form $X_t|X_0$ when we need to emphasize this dependence.

In applications one is typically interested in evaluating quantities of interest, QoI, of the form

$$(2.4) \quad \text{QoI} = \int_{\mathbb{R}^d} F(\mathbf{x}_t) p_{X_t}(\mathbf{x}_t) d\mathbf{x}_t,$$

where F denotes a physical property of the system, and p_{X_t} is the probability density of the final state. Because of the dependence of the final state on the initial condition, normalizing flow strategies focusing on the distribution $p_{X_t}(\mathbf{x}_t)$, e.g., Refs. [1, 13, 7], might not be efficient since every time the initial condition changes, the evaluation of QoI requires re-training of the neural network for $p_{X_t}(\mathbf{x}_t)$ corresponding to the new initial condition.

To circumvent this problem we propose here a new method that focuses on the use of normalizing flows to create a surrogate model for the probability density $p_{X_t|X_0}(\mathbf{x}_t|\mathbf{x}_0)$, which gives the transition probability of being at \mathbf{x}_t stating at \mathbf{x}_0 . Once a normalizing flow model is trained for $p_{X_t|X_0}(\mathbf{x}_t|\mathbf{x}_0)$, the computation of the QoI reduces to the direct evaluation of the integral

$$(2.5) \quad \text{QoI} = \int_{\mathbb{R}^d} \int_{\mathbb{R}^d} F(\mathbf{x}_t) p_{X_t|X_0}(\mathbf{x}_t|\mathbf{x}_0) p_{X_0}(\mathbf{x}_0) d\mathbf{x}_t d\mathbf{x}_0,$$

where $p_{X_0}(\mathbf{x}_0)$ denotes the probability density of the initial condition. In this approach the computational cost of evaluating QoI for different initial conditions reduces to the cost of performing a quadrature without a retraining overhead. If $\{\mathbf{x}_0^{(m)}\}$ for $i = 1 \dots M$ is a set of M -samples drawn from $p_{X_0}(\mathbf{x}_0)$, and $\{\mathbf{x}_t^{(n)}\}$ is the corresponding set of N -samples drawn from $p_{X_t|X_0}(\mathbf{x}_t|\mathbf{x}_0)$, then the quadrature can be approximated as

$$(2.6) \quad \text{QoI} \approx \frac{1}{MN} \sum_{m=1}^M \sum_{n=1}^N F(\mathbf{x}_t^{(n)}|\mathbf{x}_0^{(m)}),$$

3. The pseudo-reversible normalizing flow (PR-NF). A normalizing flow model can be viewed as a nonlinear transformation that maps an unknown target random variable, denoted by X , to a standard random variable, e.g., the standard Gaussian, denoted by Z . Because we intend to take into account the initial condition X_0 in our normalizing flow model, we define the target random variable X as

$$(3.1) \quad X := (X_0, X_t|X_0) \in \mathbb{R}^{2d}.$$

A normalizing flow model includes a forward transformation mapping X to Z and an inverse transformation mapping Z to X , i.e.,

$$(3.2) \quad Z = \mathbf{h}(X; \theta_h) \quad \text{and} \quad \hat{X} = \mathbf{g}(Z; \theta_g),$$

where θ_h, θ_g are parameters of the transformations and $\hat{X} = X$ if $\mathbf{g} = \mathbf{h}^{-1}$. The function \mathbf{h} moves (or flows) in the normalizing direction, i.e., from an unknown distribution to a standard distribution p_Z . The tradition of defining Z as the standard normal random variable $\mathcal{N}(0, \mathbb{I}_{2d})$ gives rise to the name ‘‘normalizing flow’’. Let

$p_X(\mathbf{x})$ and $p_Z(\mathbf{z})$ denote the PDF of X and Z , respectively. The relation between the two PDFs can be obtained by the change of variables formula, i.e.,

$$(3.3) \quad p_X(\mathbf{x}) = p_Z(\mathbf{z}) \left| \frac{\partial \mathbf{z}}{\partial \mathbf{x}} \right| = p_Z(\mathbf{h}(\mathbf{x})) |\det \mathbf{J}_h(\mathbf{x})|,$$

where $\det \mathbf{J}_h(\mathbf{x})$ is the determinant of the Jacobian matrix \mathbf{J}_h of the forward map $\mathbf{h}(\cdot)$.

3.1. The PR-NF model’s architecture. The PR-NF model uses the pseudo-reversible neural network architecture [10, 24, 20], i.e., $\mathbf{g} \approx \mathbf{h}^{-1}$ in Eq. (3.2), to replace the exact reversible architectures used in most existing normalizing flow models, e.g., MAF [16], Real NVPs [5]. The typical exact reversible architectures rely on functions with either triangular Jacobians or Lipschitz continuity, where the Jacobian determinant can be efficiently approximated. However, the relaxation of the reversibility condition increases the flexibility of the model design. Specifically, we define $\mathbf{h}(\cdot; \theta_h)$ and $\mathbf{g}(\cdot; \theta_g)$ as two independent fully-connected neural networks, and the pseudo-reversibility is imposed by adding a soft constraint $\|\hat{X} - X\|_2^2$ to the loss function. This architecture is different from autoencoders because the size of the bottleneck, i.e., the dimension of Z , is the same as the dimension of X and \hat{X} . Figure 1 illustrates the performance of the PR-NF on a standard two-dimensional dataset. We observe that the left panel (i.e., the true distribution) and the right panel (i.e., the PR-NF generated distribution) have a good agreement, meaning the relaxation of the reversibility does not cause a significant error.

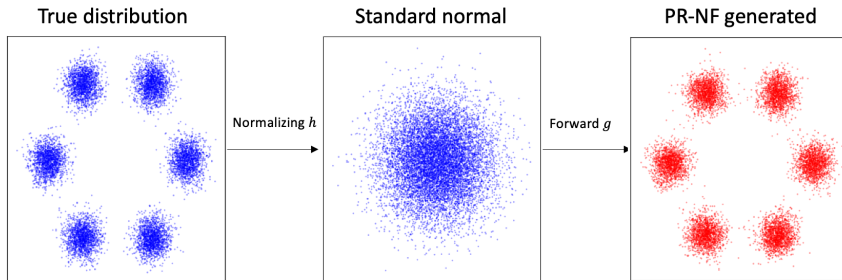


FIG. 1. Illustration of the PR-NF’s performance. The function \mathbf{h} maps the true distribution (left) to the standard normal distribution (middle), and the function \mathbf{g} generates new samples of the true distribution. We observe that the left panel and the right panel have a good agreement, meaning the relaxation of the reversibility does not cause a significant error.

The novelty of the PR-NF model is to learn the conditional distribution in Eq. (2.5), such that we can use the trained PR-NF model to compute the QoI in Eq. (2.5) for arbitrary initial conditions, $p_{X_0}(\mathbf{x}_0)$, without re-training. The key ingredient is to include the initial state X_0 into the input of the PR-NF model, i.e., Eq. (3.1). The network architecture is shown in Figure 2. Specifically, the mapping $\mathbf{h}(\cdot)$ consists of two components, i.e., $\mathbf{h}(\mathbf{x}_0, \mathbf{x}_t | \mathbf{x}_0) = (\mathbf{h}_0(\mathbf{x}_0), \mathbf{h}_1(\mathbf{x}_0, \mathbf{x}_t | \mathbf{x}_0; \theta_h))$, where $\mathbf{h}_1(\mathbf{x}_0, \mathbf{x}_t | \mathbf{x}_0; \theta_h) : \mathbb{R}^{2d} \mapsto \mathbb{R}^d$ is a fully connected neural network with tuning parameter θ_h , and $\mathbf{h}_0(\mathbf{x}_0) : \mathbb{R}^d \mapsto \mathbb{R}^d$ is an identity mapping depending only on \mathbf{x}_0 . We emphasize that it is critical to include \mathbf{x}_0 as one input of \mathbf{h}_1 to characterize the conditional distribution $p_{X_t | X_0}(\mathbf{x}_t | \mathbf{x}_0)$. We denote by \mathbf{z}_0 the output of $\mathbf{h}_0(\mathbf{x}_0)$ and \mathbf{z}_t the output of $\mathbf{h}_1(\mathbf{x}_0, \mathbf{x}_t | \mathbf{x}_0; \theta_h)$. The inverse map \mathbf{g} has a similar structure as the forward map, i.e., $\mathbf{g}(\mathbf{z}_0, \mathbf{z}_t) = (\mathbf{g}_0(\mathbf{z}_0), \mathbf{g}_1(\mathbf{z}_0, \mathbf{z}_t; \theta_g))$, where \mathbf{g}_0 is an identity map and \mathbf{g}_1 is a fully connected neural network with tuning parameter θ_g . We denote by $\hat{\mathbf{x}}_0$

and $\hat{\mathbf{x}}_t$ the outputs of \mathbf{g}_0 and \mathbf{g}_1 , respectively. Note that $\hat{\mathbf{x}}_0 = \mathbf{z}_0 = \mathbf{x}_0$ because \mathbf{h}_0 and \mathbf{g}_0 are identity maps.

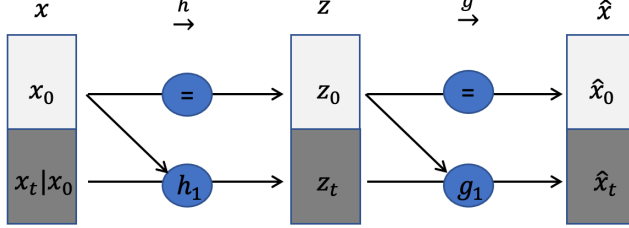


FIG. 2. The network architecture of the proposed PR-NF model.

3.2. The loss function. The loss function is defined based on a training data set, i.e.,

$$(3.4) \quad \mathcal{V}_{\text{train}} = \left\{ \mathbf{x}^{(n)} \right\}_{n=1}^N = \left\{ \mathbf{x}_0^{(n)}, \mathbf{x}_t^{(n)} | \mathbf{x}_0^{(n)} \right\}_{n=1}^N,$$

where $\{\mathbf{x}_0^{(n)}\}_{n=1}^N$ is generated from the uniform distribution over the bounded domain \mathcal{D} in Eq. (2.1). For each initial state $\mathbf{x}_0^{(n)}$, we numerically solve the SDE in Eq. (2.1) to obtain the sample $\mathbf{x}_t^{(n)} | \mathbf{x}_0^{(n)}$. The loss function consists of two components, i.e.,

$$(3.5) \quad \mathcal{L} = \mathcal{L}_1 + \lambda \mathcal{L}_2,$$

where \mathcal{L}_1 is the negative log-likelihood loss defined by

$$(3.6) \quad \mathcal{L}_1 = -\frac{1}{N} \sum_{n=1}^N \left(\log p_{Z_t}(\mathbf{h}_1(\mathbf{x}^{(n)}; \theta_h)) + \log \left| \det \mathbf{J}_{\mathbf{h}}(\mathbf{x}^{(n)}; \theta_h) \right| \right),$$

with $p_{Z_t}(\cdot)$ the probability density function of the standard normal distribution, and \mathcal{L}_2 is the pseudo-reversibility loss that measures the difference between \mathbf{x} and $\hat{\mathbf{x}}$, i.e.,

$$(3.7) \quad \mathcal{L}_2 = \frac{1}{N} \sum_{n=1}^N \left(\left\| \mathbf{x}^{(n)} - \mathbf{g}(\mathbf{h}(\mathbf{x}^{(n)}; \theta_h); \theta_g) \right\|_2^2 + \left| \det \mathbf{J}_{\mathbf{g}}(\mathbf{h}(\mathbf{x}^{(n)})) \det \mathbf{J}_{\mathbf{h}}(\mathbf{x}^{(n)}) - 1 \right| \right),$$

and λ is a hyperparameter that will be discussed in Section 3.3.

The Jacobian determinant in \mathcal{L}_1 can be written as

$$(3.8) \quad |\det \mathbf{J}_{\mathbf{h}}(\mathbf{x})| = \left| \det \begin{pmatrix} \mathbb{I}_d & 0 \\ \frac{\partial \mathbf{z}_t}{\partial \mathbf{x}_0} & \frac{\partial \mathbf{z}_t}{\partial \mathbf{x}_t} \end{pmatrix} \right| = \left| \det \left(\frac{\partial \mathbf{z}_t}{\partial \mathbf{x}_t} \right) \right|,$$

where \mathbb{I}_d is a $d \times d$ identity matrix. The simplification in Eq. (3.8) is based on the fact \mathbf{h}_0 is an identity map with respect to \mathbf{x}_0 . Thus, although we doubled the size of the input of the PR-NF model, the size of the Jacobian matrix is still $d \times d$. The proposed PR-NF has $\mathcal{O}(d^3)$ complexity in Jacobian determinant computation. However, we observe that it is not a bottleneck with GPU-accelerated linear algebra libraries in Pytorch and TensorFlow, especially for a wide range of physical processes, i.e., the examples in Section 5, in the phase space with dimension up to six.

3.3. Hyperparameter tuning. The hyperparameter λ in Eq. (3.5) determines the importance of the reversibility loss \mathcal{L}_2 . Thus, a hyperparameter tuning is needed to achieve a good performance. In this work, we will perform grid search and use the cross-entropy as a metric to find the best value for λ . Specifically, we will generate a set of candidates, denoted by $\{\lambda_j\}_{j=1}^J$. For each λ_j , we train one PR-NF model, denoted by $(\mathbf{h}^{(j)}(\mathbf{x}), \mathbf{g}^{(j)}(\mathbf{z}))$. Then, we generate M samples of $\hat{\mathbf{x}}$ by running the inverse mapping, i.e.,

$$(3.9) \quad \left\{ \hat{\mathbf{x}}^{(j,m)} = \mathbf{g}^{(j)}(\mathbf{z}^{(m)}), m = 1, \dots, M \right\},$$

where $\{\mathbf{z}^{(m)}\}_{m=1}^M = \{\mathbf{z}_0^{(m)}, \mathbf{z}_t^{(m)}\}_{m=1}^M$ with $\mathbf{z}_0^{(m)}$ generated uniformly from \mathcal{D} and $\mathbf{z}_t^{(m)}$ generated from the standard normal distribution. Because it does not require solving the SDE in Eq. (2.1), we can generate a large number of samples. Next, we build a kernel density estimator using the samples in Eq. (3.9), and compute the cross-entropy by

$$(3.10) \quad H(\lambda_j) = -\frac{1}{N} \sum_{n=1}^N \log(p_{\text{KDE}}(\mathbf{x}_t^{(n)})),$$

where p_{KDE} is the kernel density estimator based on the samples in Eq. (3.9) and $\{\mathbf{x}_t^{(n)}\}_{n=1}^N$ is the training data set in Eq. (3.4). The optimal hyperparameter λ is obtained by minimizing the cross-entropy, i.e., $\lambda = \operatorname{argmin} H(\lambda_j)$.

3.4. Discussion on the computational cost. The algorithmic cost of sampling methods consists of two parts, the ‘‘offline cost’’ and the ‘‘online cost’’. The offline cost of an algorithm represents the running time for the training process. It is determined by the architecture of the neural network, the optimizer (numerical scheme), the size of the training dataset and the number of training epochs (‘‘time’’ steps). An epoch in machine learning means one complete pass of the training dataset through the algorithm. We choose the number of epochs such that the loss function stably attains the minimum. The Monte Carlo method for sampling has no training process. However, it needs to be run repeatedly for each new initial condition. The PR-NF model is a generative model where the offline cost accounts for most of the total algorithmic cost. However, the offline cost is a one-time cost (no additional training is needed for future simulations). We denote the offline cost of the PR-NF method as C_{offline} . It is easy to utilize the GPU architecture to accelerate the computation for the training process under the PyTorch machine learning framework.

The online cost is the computational cost for sampling. Although the Monte Carlo method is conceptually simple and algorithmically straightforward, the associated computational cost can be staggeringly high. In general, the method requires many samples to get a good approximation, which may incur an arbitrarily large total runtime if the processing time of a single sample is high [22]. In contrast, the PR-NF model is a transformation that maps samples from the standard normal distribution to the distribution of interest. For an initial distribution, the computational cost of the MC method is significantly greater than the online cost of the PR-NF method because it involves the sampling and numerical integration of the SDE in Eq. (2.1). The computational cost depends on how many samples need to generate. We denote C_{MC} and $C_{\text{PR-NF}}$ as the computational cost of an initial distribution for MC and PR-NF methods, respectively. We have $C_{\text{MC}} \gg C_{\text{PR-NF}}$. To test N_{init} different initial distributions, the cost of the PR-NF method $\mathcal{O}(C_{\text{offline}} + C_{\text{PR-NF}} \times N_{\text{init}})$ is cheaper than the MC method $\mathcal{O}(C_{\text{MC}} \times N_{\text{init}})$ when N_{init} is large.

4. Convergence analysis of the PR-NF model. This section provides the convergence analysis of the pseudo-reversible normalizing flow (PR-NF) model in Section 3. For notational simplicity, the target random variable and its probability density function are denoted by X and $p_X(\mathbf{x})$, respectively. Here, we limit our attention to single-hidden-layer neural networks. The work in [15] shows that for any pair of well-behaved¹ distributions $p_X(\mathbf{x})$ and $p_Z(\mathbf{z})$, there exists a diffeomorphism $\mathbf{z} = \mathbf{f}(\mathbf{x}) = (f_1(\mathbf{x}), \dots, f_d(\mathbf{x}))$ that can transform $p_X(\mathbf{x})$ to $p_Z(\mathbf{z})$, i.e.,

$$(4.1) \quad p_X(\mathbf{x}) = p_Z(\mathbf{f}(\mathbf{x})) |\det \mathbf{J}_{\mathbf{f}}(\mathbf{x})|.$$

The proposed PR-NF model can be viewed as an approximation of the diffeomorphism, where $\mathbf{h}(\mathbf{x})$ and $\mathbf{g}(\mathbf{z})$ in Eq. (3.2) approximate \mathbf{f} and \mathbf{f}^{-1} , respectively.

We study the convergence of the PR-NF model in three stages. Section 4.1 shows the existence of a convergent neural network approximations to the target diffeomorphism \mathbf{f} by exploiting the universal approximation theorem of fully connected neural networks. Section 4.2 shows that the convergence of the loss functions \mathcal{L}_1 and \mathcal{L}_2 in Eq. (3.5) is a necessary condition to obtain the convergent approximation discussed in Section 4.1, which verifies that appropriateness of the loss function used to train the PR-NF model. Section 4.3 shows that the convergence of \mathcal{L}_1 and \mathcal{L}_2 plus some mild assumptions on the \mathbf{h} and \mathbf{g} is sufficient to ensure the convergence of the KL divergence between the true and the approximate probability density function.

4.1. Existence of a convergent approximation to the diffeomorphism.

ASSUMPTION 4.1. *We assume that the determinant of the Jacobian matrix and any partial derivative of $\mathbf{f} \in C^1(\mathbb{R}^d)$ are bounded, i.e.,*

$$(4.2) \quad \left| \frac{\partial f_i(\mathbf{x})}{\partial x_j} \right| < A_1 < \infty, \quad |\det \mathbf{J}_{\mathbf{f}}(\mathbf{x})| > A_2 > 0,$$

where A_1 and A_2 are positive constants and $i, j \in \{1, \dots, d\}$. Additionally, the probability density function $p_X(\mathbf{x})$ is bounded and all the conditional probabilities are differentiable. There exists a positive constant K such that

$$(4.3) \quad p_X(\mathbf{x}) < A_3 \exp(-\alpha \|\mathbf{x}\|^2) \text{ for } \|\mathbf{x}\| > K,$$

where $\alpha > 0$ and $A_3 > 0$ are positive constants and $\|\mathbf{x}\|$ denotes the l^2 norm.

Under Assumption 4.1, Lemma 4.2 and Lemma 4.3 demonstrate the existence and reversibility of convergent flows \mathbf{h} and \mathbf{g} , respectively. To proceed, we introduce some multivariate notations: \mathbb{Z}_+^d denote the lattice of nonnegative multi-integers in \mathbb{R}^d . For $\mathbf{m} = (m_1, \dots, m_d) \in \mathbb{Z}_+^d$, we set $|\mathbf{m}| = m_1 + \dots + m_d$, $\mathbf{x}^{\mathbf{m}} = x_1^{m_1} \dots x_d^{m_d}$, and $D^{\mathbf{m}} = \frac{\partial^{|\mathbf{m}|}}{\partial x_1^{m_1} \dots \partial x_d^{m_d}}$. We also define

$$C^k(\Omega) := \{ \mathbf{f} : D^{\mathbf{m}} f_i \in C(\Omega) \text{ for all } i \in \{1, \dots, d\}, \text{ and } |\mathbf{m}| \leq k \}.$$

LEMMA 4.2 (Theorem 4.1 in [18]). *For any given $\varepsilon > 0$, there exists a single-hidden-layer neural network $\mathbf{h} = (h_1, \dots, h_d)$ with sufficient number of neurons to approximate a function $\mathbf{f} \in C^k(\mathbb{R}^d)$ in a compact set $\Omega \subset \mathbb{R}^d$ such that*

$$(4.4) \quad \max_{\mathbf{x} \in \Omega} |D^{\mathbf{m}} f_i(\mathbf{x}) - D^{\mathbf{m}} h_i(\mathbf{x})| < \varepsilon,$$

for all $i \in \{1, \dots, d\}$ and $\mathbf{m} \in \mathbb{Z}_+^d$ with $|\mathbf{m}| \leq k$.

¹A well-behaved distribution $p_X(\mathbf{x})$ means that $p_X(\mathbf{x}) > 0$ for all $\mathbf{x} \in \mathbb{R}^d$, and all conditional probabilities $\Pr(X_i \leq x_i | \mathbf{x}_{<i})$ are differentiable, for $i = 1, 2, \dots, d$.

LEMMA 4.3. *Under Assumption 4.1 and Lemma 4.2, the flow \mathbf{h} approximating $\mathbf{f} \in C^k(\mathbb{R}^d)$ is invertible for sufficiently small $\varepsilon > 0$.*

Proof. Let \mathcal{S}_d be the set of all permutation of $\{1, \dots, d\}$, we have

$$(4.5) \quad |\det \mathbf{J}_{\mathbf{f}}(\mathbf{x}) - \det \mathbf{J}_{\mathbf{h}}(\mathbf{x})| = \left| \sum_{\sigma \in \mathcal{S}_d} \left(\text{sgn}(\sigma) \left(\prod_{i=1}^d \frac{\partial f_i}{\partial x_{\sigma_i}} - \prod_{i=1}^d \frac{\partial h_i}{\partial x_{\sigma_i}} \right) \right) \right| < C\varepsilon$$

for any $\mathbf{x} \in \Omega$, where the last inequality holds by Lemma 4.2 with $k = 1$. According to Eq. (4.2), we have

$$(4.6) \quad A_2 < |\det \mathbf{J}_{\mathbf{f}}(\mathbf{x})| = \left| \sum_{\sigma \in \mathcal{S}_d} \left(\text{sgn}(\sigma) \prod_{i=1}^d \frac{\partial f_i}{\partial x_{\sigma_i}} \right) \right| < CA_1^d.$$

We choose $\varepsilon < \frac{A_2}{2C}$ such that

$$(4.7) \quad |\det \mathbf{J}_{\mathbf{h}}(\mathbf{x})| \leq |\det \mathbf{J}_{\mathbf{f}}(\mathbf{x})| + |\det \mathbf{J}_{\mathbf{f}}(\mathbf{x}) - \det \mathbf{J}_{\mathbf{h}}(\mathbf{x})| < \frac{A_2}{2} + CA_1^d,$$

$$(4.8) \quad |\det \mathbf{J}_{\mathbf{h}}(\mathbf{x})| \geq |\det \mathbf{J}_{\mathbf{f}}(\mathbf{x})| - |\det \mathbf{J}_{\mathbf{f}}(\mathbf{x}) - \det \mathbf{J}_{\mathbf{h}}(\mathbf{x})| > \frac{A_2}{2} > 0.$$

By the inverse function theorem, \mathbf{h} is invertible in Ω . \square

Similarly, we can prove the invertibility of \mathbf{g} for the function \mathbf{f}^{-1} with Eq. (4.4). So far, we proved the existence of convergent neural network \mathbf{h} and \mathbf{g} to approximate \mathbf{f} and \mathbf{f}^{-1} , respectively.

4.2. Convergence of the loss function. We now prove that the convergence of the loss functions \mathcal{L}_1 and \mathcal{L}_2 in Eq. (3.5) is a necessary condition to obtain the convergent approximation discussed in Section 4.1. To proceed, we define two auxiliary random variables

$$(4.9) \quad \tilde{X} = \mathbf{h}^{-1}(Z) \quad \text{and} \quad \hat{X} = \mathbf{g}(Z),$$

where Z follows the standard normal distribution. Using the change of variables formula, the probability density functions of \tilde{X} and \hat{X} are defined by

$$(4.10) \quad p_{\tilde{X}}(\mathbf{x}) = p_Z(\mathbf{h}(\mathbf{x})) |\det \mathbf{J}_{\mathbf{h}}(\mathbf{x})|, \quad p_{\hat{X}}(\mathbf{x}) = p_Z(\mathbf{g}^{-1}(\mathbf{x})) |\det \mathbf{J}_{\mathbf{g}^{-1}}(\mathbf{x})|.$$

For simplicity, we consider the loss functions in the continuous form, i.e.,

$$(4.11) \quad \mathcal{L}_1 = - \int_{\mathbb{R}^d} p_X(\mathbf{x}) \log p_{\tilde{X}}(\mathbf{x}) d\mathbf{x},$$

and

$$(4.12) \quad \mathcal{L}_2 = \int_{\Omega} p_X(\mathbf{x}) (\|\mathbf{g}(\mathbf{h}(\mathbf{x})) - \mathbf{x}\|^2 + |\det \mathbf{J}_{\mathbf{g}}(\mathbf{h}(\mathbf{x})) \det \mathbf{J}_{\mathbf{h}}(\mathbf{x}) - 1|) d\mathbf{x},$$

where Ω is a compact set. For the variables \tilde{X} and \hat{X} , we have the following assumptions.

ASSUMPTION 4.4. *We assume the density functions $p_X(\mathbf{x})$ and $p_{\tilde{X}}(\mathbf{x})$ satisfy*

$$(4.13) \quad A_4 \exp(-\alpha \|\mathbf{x}\|^2) < \frac{p_X(\mathbf{x})}{p_{\tilde{X}}(\mathbf{x})} < A_4 \exp(\alpha \|\mathbf{x}\|^2),$$

where α and A_4 are positive constants.

Lemma 4.5 and Theorems 4.6, 4.7 below will demonstrate that both \mathcal{L}_1 and \mathcal{L}_2 will approach the optimal constants in this case, with a difference between the loss and the optimal constant of the order $O(\varepsilon)$.

LEMMA 4.5. *For arbitrarily small $\varepsilon > 0$, there exists a random variable \tilde{X} with the density function $p_{\tilde{X}}(\mathbf{x})$ defined in Eq. (4.10) such that*

$$(4.14) \quad |p_X(\mathbf{x}) - p_{\tilde{X}}(\mathbf{x})| < C\varepsilon, \quad \text{for } \mathbf{x} \in \Omega,$$

where $\Omega \subseteq \mathbb{R}^d$ is a compact set and $C > 0$ is a constant.

Proof. By Lemma 4.2 with $k = 0$, for any $\mathbf{x} \in \Omega$ we have

$$(4.15) \quad \|\mathbf{f}(\mathbf{x}) - \mathbf{h}(\mathbf{x})\| = \sqrt{\sum_{i=1}^d |f_i(\mathbf{x}) - h_i(\mathbf{x})|^2} < C\varepsilon.$$

The standard normal random variable $Z \in \mathbb{R}^d$ has bounded gradient, i.e., $\|\nabla p_Z(\mathbf{z})\| < C$ for any $\mathbf{z} \in \mathbb{R}^d$. Applying the mean value theorem, we have

$$(4.16) \quad |p_Z(\mathbf{f}(\mathbf{x})) - p_Z(\mathbf{h}(\mathbf{x}))| = |\nabla p_Z(\xi) \cdot (\mathbf{f}(\mathbf{x}) - \mathbf{h}(\mathbf{x}))| \leq \|\nabla p_Z(\xi)\| \|\mathbf{f}(\mathbf{x}) - \mathbf{h}(\mathbf{x})\| < C\varepsilon,$$

where ξ is between $\mathbf{f}(\mathbf{x})$ and $\mathbf{h}(\mathbf{x})$, ε is given in Lemma 4.2 and $C > 0$ is a constant. Because Z has bounded density function, we can exploit Eqs. (4.5), (4.7), (4.16) to derive

$$(4.17) \quad \begin{aligned} & |p_X(\mathbf{x}) - p_{\tilde{X}}(\mathbf{x})| \\ &= |p_Z(\mathbf{f}(\mathbf{x}))| \det \mathbf{J}_f(\mathbf{x}) - p_Z(\mathbf{h}(\mathbf{x}))| \det \mathbf{J}_h(\mathbf{x})| \\ &= |p_Z(\mathbf{f}(\mathbf{x}))| (|\det \mathbf{J}_f(\mathbf{x})| - |\det \mathbf{J}_h(\mathbf{x})|) + |\det \mathbf{J}_h(\mathbf{x})| (|p_Z(\mathbf{f}(\mathbf{x})) - p_Z(\mathbf{h}(\mathbf{x}))|) \\ &\leq |p_Z(\mathbf{f}(\mathbf{x}))| |\det \mathbf{J}_f(\mathbf{x}) - \det \mathbf{J}_h(\mathbf{x})| + |\det \mathbf{J}_h(\mathbf{x})| |p_Z(\mathbf{f}(\mathbf{x})) - p_Z(\mathbf{h}(\mathbf{x}))| < C\varepsilon \end{aligned}$$

for any $\mathbf{x} \in \Omega$ which concludes the proof. \square

Based on the results from Lemma 4.5, we have the convergence of the continuous loss function \mathcal{L}_1 defined in Eq. (4.11).

THEOREM 4.6. *For arbitrarily small $\varepsilon > 0$, there exists a random variable \tilde{X} with the density function $p_{\tilde{X}}(\mathbf{x})$ in Eq. (4.10) such that \mathcal{L}_1 has the bound*

$$(4.18) \quad - \int_{\mathbb{R}^d} p_X(\mathbf{x}) \log p_X(\mathbf{x}) d\mathbf{x} \leq \mathcal{L}_1 < - \int_{\mathbb{R}^d} p_X(\mathbf{x}) \log p_X(\mathbf{x}) d\mathbf{x} + \varepsilon.$$

Proof. Using the inequality $\log t \leq t - 1$ for all $t > 0$, we have

$$(4.19) \quad \begin{aligned} - \int_{\mathbb{R}^d} p_X(\mathbf{x}) \log p_X(\mathbf{x}) d\mathbf{x} - \mathcal{L}_1 &= \int_{\mathbb{R}^d} p_X(\mathbf{x}) \log \frac{p_{\tilde{X}}(\mathbf{x})}{p_X(\mathbf{x})} d\mathbf{x} \\ &\leq \int_{\mathbb{R}^d} p_X(\mathbf{x}) \left(\frac{p_{\tilde{X}}(\mathbf{x})}{p_X(\mathbf{x})} - 1 \right) d\mathbf{x} \\ &= \int_{\mathbb{R}^d} p_{\tilde{X}}(\mathbf{x}) - p_X(\mathbf{x}) d\mathbf{x} = 0. \end{aligned}$$

To prove the right side of Eq. (4.18), we need to show that

$$(4.20) \quad \int_{\mathbb{R}^d} p_X(\mathbf{x}) \log \frac{p_X(\mathbf{x})}{p_{\tilde{X}}(\mathbf{x})} d\mathbf{x} < \varepsilon.$$

We define $B_d(r) := \{\mathbf{x} \in \mathbb{R}^d : \|\mathbf{x}\| \leq r\}$ and $V_{d-1}(r)$ be the volume of $\{\mathbf{x} \in \mathbb{R}^d : \|\mathbf{x}\| = r\}$. For every $\varepsilon_1 < \min\{A_3 \exp(-\alpha), A_3 \exp(-\alpha K^2)\}$, K is the constant in Assumption 4.1, we let $K_1 = \sqrt{-\frac{1}{\alpha} \log \frac{\varepsilon_1}{A_3}}$, then $K_1 > \max\{1, K\}$. According to Eq. (4.3) in Assumption 4.1, $p_X(\mathbf{x}) < A_3 \exp(-\alpha \|\mathbf{x}\|^2) \leq \varepsilon_1$ over the domain $B_d(K_1)^c$. Define $\Omega_{\varepsilon_1} := \{\mathbf{x} : p_X(\mathbf{x}) \geq \varepsilon_1\}$, then Ω_{ε_1} is contained in $B_d(K_1)$. Since $p_X(\mathbf{x})$ is continuous, Ω_{ε_1} is closed. Moreover, as a bounded closed set in \mathbb{R}^d , Ω_{ε_1} is compact. The KL divergence between distributions p_X and $p_{\tilde{X}}$ has the following bound

$$\begin{aligned}
D_{\text{KL}}(p_X \parallel p_{\tilde{X}}) &= \int_{\mathbb{R}^d} p_X(\mathbf{x}) \log \frac{p_X(\mathbf{x})}{p_{\tilde{X}}(\mathbf{x})} d\mathbf{x} \\
&\leq \int_{p_X(\mathbf{x}) \geq \varepsilon_1} p_X(\mathbf{x}) \log \frac{p_X(\mathbf{x})}{p_{\tilde{X}}(\mathbf{x})} d\mathbf{x} \\
(4.21) \quad &+ \int_{\{p_X(\mathbf{x}) < \varepsilon_1\} \cap B_d(K_1)} p_X(\mathbf{x}) \log \frac{p_X(\mathbf{x})}{p_{\tilde{X}}(\mathbf{x})} d\mathbf{x} \\
&+ \int_{\{p_X(\mathbf{x}) < \varepsilon_1\} \cap B_d(K_1)^c} p_X(\mathbf{x}) \log \frac{p_X(\mathbf{x})}{p_{\tilde{X}}(\mathbf{x})} d\mathbf{x} \\
&:= I_1 + I_2 + I_3.
\end{aligned}$$

Next we investigate all terms on the right side of Eq. (4.21). By Lemma 4.5, for every $\varepsilon_2 > 0$, there exists variable \tilde{X} such that

$$(4.22) \quad |p_X(\mathbf{x}) - p_{\tilde{X}}(\mathbf{x})| < C\varepsilon_2,$$

for any $\mathbf{x} \in \Omega_{\varepsilon_1}$. Choosing $\varepsilon_2 < \frac{\varepsilon_1}{2C}$, we have $p_{\tilde{X}}(\mathbf{x}) > \varepsilon_1/2$ for the case $p_X(\mathbf{x}) \geq \varepsilon_1$. Applying the mean value theorem, I_1 has the bound

$$\begin{aligned}
I_1 &= \int_{p_X(\mathbf{x}) \geq \varepsilon_1} p_X(\mathbf{x}) (\log(p_X(\mathbf{x})) - \log(p_{\tilde{X}}(\mathbf{x}))) d\mathbf{x} \\
(4.23) \quad &\leq \int_{p_X(\mathbf{x}) \geq \varepsilon_1} p_X(\mathbf{x}) \left| \frac{1}{\xi} \right| |p_X(\mathbf{x}) - p_{\tilde{X}}(\mathbf{x})| d\mathbf{x} \\
&\leq \frac{2C\varepsilon_2}{\varepsilon_1} \int_{p_X(\mathbf{x}) \geq \varepsilon_1} p_X(\mathbf{x}) d\mathbf{x} \leq \frac{2C\varepsilon_2}{\varepsilon_1},
\end{aligned}$$

where $\left| \frac{1}{\xi} \right| \leq \frac{2}{\varepsilon_1}$ because ξ is between $p_X(\mathbf{x})$ and $p_{\tilde{X}}(\mathbf{x})$. Since we define $\varepsilon_2 < \frac{\varepsilon_1}{2C}$, we are able to let $\varepsilon_2/\varepsilon_1 \rightarrow 0$ to guarantee $I_1 \rightarrow 0$.

Positive density functions $p_X(\mathbf{x})$, $p_{\tilde{X}}(\mathbf{x})$ are continuous, thus $\log \frac{p_X(\mathbf{x})}{p_{\tilde{X}}(\mathbf{x})}$ is continuous and bounded over $B_d(K)$, i.e., $\log \frac{p_X(\mathbf{x})}{p_{\tilde{X}}(\mathbf{x})} < C_1$ for $\mathbf{x} \in B_d(K)$. By Eq. (4.13) in Assumption 4.1, it follows that $\log \frac{p_X(\mathbf{x})}{p_{\tilde{X}}(\mathbf{x})} < C_2 K_1^2$ for $\mathbf{x} \in B_d(K_1) \setminus B_d(K)$. Hence,

$\log \frac{p_X(\mathbf{x})}{p_{\tilde{X}}(\mathbf{x})} < \max\{C_1, C_2 K_1^2\}$ for $\mathbf{x} \in B_d(K_1)$. The term I_2 has the bound

$$\begin{aligned}
 (4.24) \quad I_2 &= \int_{\{p_X(\mathbf{x}) < \varepsilon_1\} \cap B_d(K_1)} p_X(\mathbf{x}) \log \frac{p_X(\mathbf{x})}{p_{\tilde{X}}(\mathbf{x})} d\mathbf{x} \\
 &\leq \int_{\{p_X(\mathbf{x}) < \varepsilon_1\} \cap B_d(K_1)} \left| p_X(\mathbf{x}) \log \frac{p_X(\mathbf{x})}{p_{\tilde{X}}(\mathbf{x})} \right| d\mathbf{x} \\
 &\leq C \varepsilon_1 \int_{B_d(K_1)} \max\{1, K_1^2\} d\mathbf{x} \\
 &= C \varepsilon_1 \frac{\pi^{d/2}}{\Gamma(d/2 + 1)} \max\{K_1^d, K_1^{d+2}\} \\
 &\leq C \max\{\varepsilon_1 (\log \frac{\varepsilon_1}{A_1})^{d/2}, \varepsilon_1 (\log \frac{\varepsilon_1}{A_1})^{d/2+1}\},
 \end{aligned}$$

where C is a constant and $I_2 \rightarrow 0$ as $\varepsilon_1 \rightarrow 0$. The last inequality holds due to $K_1 = \sqrt{-\frac{1}{\alpha} \log \frac{\varepsilon_1}{A_1}}$. Lastly we have the bound for I_3

$$\begin{aligned}
 (4.25) \quad I_3 &= \int_{\{p_X(\mathbf{x}) < \varepsilon_1\} \cap B_d(K_1)^c} p_X(\mathbf{x}) \log \frac{p_X(\mathbf{x})}{p_{\tilde{X}}(\mathbf{x})} d\mathbf{x} \\
 &= \int_{B_d(K_1)^c} p_X(\mathbf{x}) \log \frac{p_X(\mathbf{x})}{p_{\tilde{X}}(\mathbf{x})} d\mathbf{x} \\
 &\leq C \int_{B_d(K_1)^c} \exp(-\alpha \|\mathbf{x}\|^2) \|\mathbf{x}\|^2 d\mathbf{x}.
 \end{aligned}$$

According to the identity $\int_{B_d(R_2) \setminus B_d(R_1)} y(\|\mathbf{x}\|) d\mathbf{x} = V_{d-1}(1) \int_{R_1}^{R_2} y(r) r^{d-1} dr$, we have

$$\begin{aligned}
 (4.26) \quad I_3 &\leq C V_{d-1}(1) \int_{K_1}^{+\infty} \exp(-\alpha r^2) r^2 r^{d-1} dr \\
 &= C \int_{K_1}^{+\infty} \exp(-\alpha r^2) r^{d+1} dr \\
 &= C \left(\left[\frac{\exp(-\alpha r^2) r^d}{-2\alpha} \right]_{K_1}^{+\infty} + \frac{d+1}{2\alpha} \int_{K_1}^{+\infty} \exp(-\alpha r^2) r^d dr \right) \\
 &= C \left(\left[\frac{\exp(-\alpha r^2) r^d}{-2\alpha} \right]_{K_1}^{+\infty} + \dots + \frac{(d+1)!}{(2\alpha)^{d+1}} \int_{K_1}^{+\infty} \exp(-\alpha r^2) dr \right),
 \end{aligned}$$

where $I_3 \rightarrow 0$ as $K_1 \rightarrow +\infty$. Since $K_1 = \sqrt{-\frac{1}{\alpha} \log \frac{\varepsilon_1}{A_1}}$, we have $I_3 \rightarrow 0$ as $\varepsilon_1 \rightarrow 0$. \square

In summary, Theorem 4.6 shows that the loss function \mathcal{L}_1 converges to the entropy of $p_X(\mathbf{x})$ as \mathbf{h} converges to \mathbf{f} . The following Theorem 4.7 proves the convergence of the continuous loss function \mathcal{L}_2 as defined in Eq. (4.12).

THEOREM 4.7. *For arbitrarily small $\varepsilon > 0$, there exists a single-hidden-layer neural network \mathbf{g} such that*

$$(4.27) \quad \mathcal{L}_2 < \varepsilon,$$

in any compact set $\Omega \subseteq \mathbb{R}^d$.

Proof. By Assumption 4.1, p_X is bounded. \mathcal{L}_2 has the following bound:

$$\begin{aligned}
\mathcal{L}_2 &= \int_{\Omega} p_X(\mathbf{x}) \left(\|\mathbf{g}(\mathbf{h}(\mathbf{x})) - \mathbf{x}\|^2 d\mathbf{x} + \int_{\Omega} |\det \mathbf{J}_{\mathbf{g}}(\mathbf{h}(\mathbf{x})) \det \mathbf{J}_{\mathbf{h}}(\mathbf{x}) - 1| \right) d\mathbf{x} \\
&\leq C \int_{\Omega} \|\mathbf{g}(\mathbf{h}(\mathbf{x})) - \mathbf{x}\|^2 d\mathbf{x} + \int_{\Omega} |\det \mathbf{J}_{\mathbf{g}}(\mathbf{h}(\mathbf{x})) \det \mathbf{J}_{\mathbf{h}}(\mathbf{x}) - 1| d\mathbf{x} \\
&= C \left(\int_{\Omega} \|\mathbf{g}(\mathbf{h}(\mathbf{x})) - \mathbf{h}^{-1}(\mathbf{h}(\mathbf{x}))\|^2 d\mathbf{x} \right. \\
(4.28) \quad &\quad \left. + \int_{\Omega} |\det \mathbf{J}_{\mathbf{g}}(\mathbf{h}(\mathbf{x})) (\det \mathbf{J}_{\mathbf{h}^{-1}}(\mathbf{h}(\mathbf{x})))^{-1} - 1| d\mathbf{x} \right) \\
&= C \left(\int_{\mathbf{h}(\Omega)} \|\mathbf{g}(\mathbf{y}) - \mathbf{h}^{-1}(\mathbf{y})\|^2 |\det \mathbf{J}_{\mathbf{h}^{-1}}(\mathbf{y})| d\mathbf{y} \right. \\
&\quad \left. + \int_{\mathbf{h}(\Omega)} |\det \mathbf{J}_{\mathbf{g}}(\mathbf{y}) - \det \mathbf{J}_{\mathbf{h}^{-1}}(\mathbf{y})| d\mathbf{y} \right) := C(I_1 + I_2).
\end{aligned}$$

Since \mathbf{h} is continuous in a compact set Ω , by the extreme value theorem, \mathbf{h} is bounded in Ω , i.e., there exists a constant M such that $|\mathbf{h}(\mathbf{x})| \leq M$ for all $\mathbf{x} \in \Omega$. Therefore, $\mathbf{h}(\Omega) \subseteq B_d(M)$. Let \mathbf{g} be the approximation of \mathbf{h}^{-1} , and the term I_1 has the bound

$$\begin{aligned}
(4.29) \quad I_1 &= \int_{\mathbf{h}(\Omega)} \|\mathbf{g}(\mathbf{y}) - \mathbf{h}^{-1}(\mathbf{y})\|^2 |\det \mathbf{J}_{\mathbf{h}^{-1}}(\mathbf{y})| d\mathbf{y} \\
&\leq \int_{B_d(M)} \|\mathbf{g}(\mathbf{y}) - \mathbf{h}^{-1}(\mathbf{y})\|^2 |\det \mathbf{J}_{\mathbf{h}^{-1}}(\mathbf{y})| d\mathbf{y} \\
&= \int_{B_d(M)} \left(\sum_{i=1}^d |g_i(\mathbf{y}) - h_i^{-1}(\mathbf{y})|^2 \right) |\det \mathbf{J}_{\mathbf{h}^{-1}}(\mathbf{y})| d\mathbf{y} \leq \int_{B_d(M)} d\varepsilon_1^2 C d\mathbf{y} \leq C\varepsilon_1^2,
\end{aligned}$$

where the last inequality holds by Lemma 4.2 with $k = 0$ and the determinate of Jacobian of \mathbf{h}^{-1} has the upper bound in Eq. (4.8). Let \mathcal{S}_d be the set of all permutation of $\{1, \dots, d\}$, we have

$$(4.30) \quad |\det \mathbf{J}_{\mathbf{g}}(\mathbf{y}) - \det \mathbf{J}_{\mathbf{h}^{-1}}(\mathbf{y})| = \left| \sum_{\sigma \in \mathcal{S}_d} \left(\text{sgn}(\sigma) \left(\prod_{i=1}^d \frac{\partial g_i(\mathbf{y})}{\partial x_{\sigma_i}} - \prod_{i=1}^d \frac{\partial h_i^{-1}(\mathbf{y})}{\partial x_{\sigma_i}} \right) \right) \right| < C\varepsilon_1$$

for any $\mathbf{y} \in B_d(M)$, where the last inequality holds by Lemma 4.2 with $k = 1$. We have the bound for I_2

$$(4.31) \quad I_2 = \int_{\mathbf{h}(\Omega)} |\det \mathbf{J}_{\mathbf{g}}(\mathbf{y}) - \det \mathbf{J}_{\mathbf{h}^{-1}}(\mathbf{y})| d\mathbf{y} \leq \int_{B_d(M)} |\det \mathbf{J}_{\mathbf{g}}(\mathbf{y}) - \det \mathbf{J}_{\mathbf{h}^{-1}}(\mathbf{y})| d\mathbf{y} \leq C\varepsilon_1.$$

The convergence of \mathcal{L}_2 to 0 as ε_1 approaches 0 is established by Eqs. (4.28), (4.29) and (4.31). By choosing ε_1 sufficiently small, we complete the proof. \square

4.3. Convergence of the KL divergence. The analysis in Section 4.2 shows that the convergence of \mathcal{L}_1 and \mathcal{L}_2 is a necessary condition necessary condition to obtain the convergent approximation discussed in Section 4.1, which verifies that appropriateness of the loss function used to train the PR-NF model. Here we show that the convergence of \mathcal{L}_1 and \mathcal{L}_2 plus some mild assumptions on the \mathbf{h} and \mathbf{g} is sufficient to ensure the convergence of the KL divergence between p_X and $p_{\hat{X}}$.

ASSUMPTION 4.8. *We assume that the target random variable X has finite second-order moment, and there exists positive constant A_5 such that*

$$(4.32) \quad \nabla p_{\widehat{X}}(\mathbf{x}) \leq A_5(\|\mathbf{x}\| + 1)p_{\widehat{X}}(\mathbf{x}),$$

where $p_{\widehat{X}}(\mathbf{x})$ is defined in Eq. (4.10).

THEOREM 4.9. *For any given $\varepsilon > 0$, under the assumptions of Theorems 4.6, 4.7 and Assumption 4.8, the KL divergence between target variable X and the approximation \widehat{X} defined in Eq. (4.9) satisfies $D_{\text{KL}}(p_X \| p_{\widehat{X}}) < \varepsilon$.*

Proof. For arbitrarily small $\varepsilon_1 > 0$, under Theorems 4.6, we have

$$(4.33) \quad \mathcal{L}_1 \leq - \int_{\mathbb{R}^d} p_X(\mathbf{x}) \log p_X(\mathbf{x}) d\mathbf{x} + \varepsilon_1,$$

and for arbitrarily small $\varepsilon_2 > 0$, under Theorems 4.7, we have

$$(4.34) \quad \mathcal{L}_2(\mathbb{R}^d) = \int_{\mathbb{R}^d} p_X(\mathbf{x}) (\|\mathbf{g}(\mathbf{h}(\mathbf{x})) - \mathbf{x}\|^2 + |\det \mathbf{J}_{\mathbf{g}}(\mathbf{h}(\mathbf{x})) \det \mathbf{J}_{\mathbf{h}}(\mathbf{x}) - 1|) d\mathbf{x} < \varepsilon_2.$$

To simplify the notation, we denote $\mathbf{M}(\mathbf{x}) := \mathbf{g}(\mathbf{h}(\mathbf{x}))$, Then Eq. (4.34) is rewritten as

$$(4.35) \quad \mathcal{L}_2(\mathbb{R}^d) = \int_{\mathbb{R}^d} p_X(\mathbf{x}) (\|\mathbf{M}(\mathbf{x}) - \mathbf{x}\|^2 + |\det \mathbf{J}_{\mathbf{M}}(\mathbf{x}) - 1|) d\mathbf{x} < \varepsilon_2.$$

Since $\widehat{X} = \mathbf{g}(Z) = \mathbf{g}(\mathbf{h}(\widetilde{X})) = \mathbf{M}(\widetilde{X})$, by the change of variables formula we have

$$(4.36) \quad p_{\widehat{X}}(\mathbf{x}) = p_{\widehat{X}}(\mathbf{M}(\mathbf{x})) |\det \mathbf{J}_{\mathbf{M}}(\mathbf{x})|.$$

The KL divergence between distributions P_X and $P_{\widehat{X}}$ has the following bound

$$(4.37) \quad \begin{aligned} D_{\text{KL}}(p_X \| p_{\widehat{X}}) &\leq \int_{\mathbb{R}^d} p_X(\mathbf{x}) \log \frac{p_X(\mathbf{x})}{p_{\widehat{X}}(\mathbf{x})} d\mathbf{x} \\ &\leq \int_{\mathbb{R}^d} p_X(\mathbf{x}) \log \frac{p_X(\mathbf{x})}{p_{\widehat{X}}(\mathbf{x})} d\mathbf{x} + \int_{\mathbb{R}^d} p_X(\mathbf{x}) \log \frac{p_{\widehat{X}}(\mathbf{x})}{p_{\widehat{X}}(\mathbf{x})} d\mathbf{x} \\ &= \int_{\mathbb{R}^d} p_X(\mathbf{x}) \log \frac{p_X(\mathbf{x})}{p_{\widehat{X}}(\mathbf{x})} d\mathbf{x} + \int_{\mathbb{R}^d} p_X(\mathbf{x}) \log \frac{p_{\widehat{X}}(\mathbf{M}(\mathbf{x})) |\det \mathbf{J}_{\mathbf{M}}(\mathbf{x})|}{p_{\widehat{X}}(\mathbf{x})} d\mathbf{x} \\ &= \int_{\mathbb{R}^d} p_X(\mathbf{x}) \log \frac{p_X(\mathbf{x})}{p_{\widehat{X}}(\mathbf{x})} d\mathbf{x} + \int_{\mathbb{R}^d} p_X(\mathbf{x}) \log \frac{p_{\widehat{X}}(\mathbf{M}(\mathbf{x}))}{p_{\widehat{X}}(\mathbf{x})} d\mathbf{x} \\ &\quad + \int_{\mathbb{R}^d} p_X(\mathbf{x}) \log |\det \mathbf{J}_{\mathbf{M}}(\mathbf{x})| d\mathbf{x} := I_1 + I_2 + I_3. \end{aligned}$$

According to Eq. (4.33), we have $I_1 < \varepsilon_1$. Apply the mean value theorem, I_2 has the bound

$$(4.38) \quad \begin{aligned} I_2 &= \int_{\mathbb{R}^d} p_X(\mathbf{x}) \log \frac{p_{\widehat{X}}(\mathbf{M}(\mathbf{x}))}{p_{\widehat{X}}(\mathbf{x})} d\mathbf{x} \\ &= \int_{\mathbb{R}^d} p_X(\mathbf{x}) \left(\log(p_{\widehat{X}}(\mathbf{M}(\mathbf{x}))) - \log(p_{\widehat{X}}(\mathbf{x})) \right) d\mathbf{x} \\ &= \int_{\mathbb{R}^d} p_X(\mathbf{x}) \left(\frac{\nabla p_{\widehat{X}}(\boldsymbol{\xi})}{p_{\widehat{X}}(\boldsymbol{\xi})} \|\mathbf{M}(\mathbf{x}) - \mathbf{x}\| \right) d\mathbf{x}, \end{aligned}$$

where $\boldsymbol{\xi}$ is between $\mathbf{M}(\mathbf{x})$ and \mathbf{x} . By Eq. (4.32) in Assumption 4.1, we have

$$\begin{aligned}
(4.39) \quad I_2 &\leq C \int_{\mathbb{R}^d} p_X(\mathbf{x})(\|\boldsymbol{\xi}\| + 1) \|\mathbf{M}(\mathbf{x}) - \mathbf{x}\| d\mathbf{x} \\
&\leq C \int_{\mathbb{R}^d} p_X(\mathbf{x})(\|\mathbf{M}(\mathbf{x}) - \mathbf{x}\| + \|\mathbf{x}\| + 1) \|\mathbf{M}(\mathbf{x}) - \mathbf{x}\| d\mathbf{x} \\
&= C \left(\int_{\mathbb{R}^d} p_X(\mathbf{x}) \|\mathbf{M}(\mathbf{x}) - \mathbf{x}\|^2 d\mathbf{x} + \int_{\mathbb{R}^d} p_X(\mathbf{x}) \|\mathbf{x}\| \|\mathbf{M}(\mathbf{x}) - \mathbf{x}\| d\mathbf{x} \right. \\
&\quad \left. + \int_{\mathbb{R}^d} p_X(\mathbf{x}) \|\mathbf{M}(\mathbf{x}) - \mathbf{x}\| d\mathbf{x} \right) \\
&\leq C \left[\varepsilon_2 + \left(\int_{\mathbb{R}^d} p_X(\mathbf{x}) \|\mathbf{x}\|^2 d\mathbf{x} \right)^{\frac{1}{2}} \left(\int_{\mathbb{R}^d} p_X(\mathbf{x}) \|\mathbf{M}(\mathbf{x}) - \mathbf{x}\|^2 d\mathbf{x} \right)^{\frac{1}{2}} \right. \\
&\quad \left. + \left(\int_{\mathbb{R}^d} p_X(\mathbf{x}) d\mathbf{x} \right)^{\frac{1}{2}} \left(\int_{\mathbb{R}^d} p_X(\mathbf{x}) \|\mathbf{M}(\mathbf{x}) - \mathbf{x}\|^2 d\mathbf{x} \right)^{\frac{1}{2}} \right] \leq C(\varepsilon_2 + \varepsilon_2^{\frac{1}{2}}).
\end{aligned}$$

Since $\log |t| \leq |t - 1|$ for every $t \in \mathbb{R}$, I_3 has the bound

$$(4.40) \quad I_3 = \int_{\mathbb{R}^d} p_X(\mathbf{x}) \log |\det \mathbf{J}_M(\mathbf{x})| d\mathbf{x} \leq \int_{\mathbb{R}^d} p_X(\mathbf{x}) |\det \mathbf{J}_M(\mathbf{x}) - 1| d\mathbf{x} \leq \varepsilon_2.$$

Therefore,

$$(4.41) \quad D_{\text{KL}}(p_X \| p_{\hat{X}}) \leq \varepsilon_1 + C(\varepsilon_2 + \varepsilon_2^{\frac{1}{2}}).$$

Let $\varepsilon_1 < \varepsilon/2$ and $\varepsilon_2 < \min\{\varepsilon^2/(16C^2), 1\}$, then we have

$$(4.42) \quad D_{\text{KL}}(p_X \| p_{\hat{X}}) \leq \varepsilon_1 + C(2\varepsilon_2^{\frac{1}{2}}) \leq \frac{\varepsilon}{2} + C \frac{\varepsilon}{2C} \leq \varepsilon.$$

Thus, $D_{\text{KL}}(p_X \| p_{\hat{X}}) \leq \varepsilon$. We complete the proof. \square

5. Numerical examples and applications. In this section we present numerical experiments demonstrating the superior performance of the PR-NF model in comparison with the standard MC method. The example in Sec.5.1 benchmarks the accuracy of our method for a problem with known analytical ground-truth solution. In Sec. 5.2 we present an application to plasma physics and in Sec.5.3 an application to fluid mechanics. Since in these cases there are not known analytical solutions, the ground-truth corresponds to MC simulations with sufficiently large samples. In all numerical simulations, the PyTorch machine learning framework has been implemented with CUDA GPU. The PR-NF model uses the Adam optimizer [11] and the Tanh activation function.

5.1. Verification of algorithm accuracy. In this subsection, we use a one-dimensional nonlinear SDE and a ten-dimensional linear SDE to verify the accuracy of the proposed algorithm. We first consider the following one-dimensional SDE

$$(5.1) \quad X_t = X_0 + \int_0^t \mathbf{b}(s, X_s) ds + \int_0^t \boldsymbol{\sigma}(s, X_s) dW_s \quad \text{with } X_0 \in [0, L],$$

where $\mathbf{b}(s, X_s) = 2\sqrt{X_s} + 1$, $\boldsymbol{\sigma}(s, X_s) = 2\sqrt{X_s}$, $L = 5$, $t = 0.1$. The analytical solution of this SDE is

$$(5.2) \quad X_t = (\sqrt{X_0} + t + W_t)^2,$$

where X_0 is the initial condition, and the corresponding conditional distribution is

$$(5.3) \quad p_{X_t|X_0}(x|x_0) = \frac{1}{2\sqrt{2\pi t x}} \left[\exp\left(\frac{-(\sqrt{x} - \sqrt{x_0} - t)^2}{2t}\right) + \exp\left(\frac{-(\sqrt{x} + \sqrt{x_0} + t)^2}{2t}\right) \right].$$

The distribution of X_t subject to an initial distribution $p_{X_0}(x_0)$ can be computed by the convolution with $p_{X_t|X_0}(x|x_0)$. Since the analytical solution is known, we use this example to test the accuracy of the propose method.

The training dataset consists of $N_{\text{train}} = 20000$ samples with initial positions $\{X_0^{(n)}\}_{n=1}^{N_{\text{train}}}$ sampled from a uniform distribution over the domain $\mathcal{D} = [0, 5]$, and terminal positions $\{X_t^{(n)}\}_{n=1}^{N_{\text{train}}}$ generated by MC simulations of Eq. (5.1). The neural network has $N_{\text{layer}} = 1$ hidden layer with $N_{\text{neuron}} = 256$ neurons. The hyperparameter λ in the loss function is selected according to the method described in Sec. 3.3. The left panel of Fig. 3 shows the cross entropy $H(\lambda)$ defined in Eq. (3.10) with different λ . As it shown, the PR-NF model attains the minimum of $H(\lambda)$ when $\lambda = 50$. The middle panel and right panel of Fig. 3 correspond to the accuracy performance of the proposed PR-NF model with two cases $\lambda = 1$ and $\lambda = 50$, respectively. The red curve is the exact density function and the histogram is synthesized by the PR-NF model. A good agreement is shown in the right panel ($\lambda = 50$). In contrast, $\lambda = 1$ is too small to guarantee the reversibility. Without the tuning process of λ , the PR-NF model may fail to balance the \mathcal{L}_1 and \mathcal{L}_2 , e.g., the middle panel of Fig. 3. The minimization of cross entropy $H(\lambda)$ in Section 3.3 is an effective and appropriate approach to choose λ . An optimal parameter λ is necessary to obtain an accurate surrogate model.

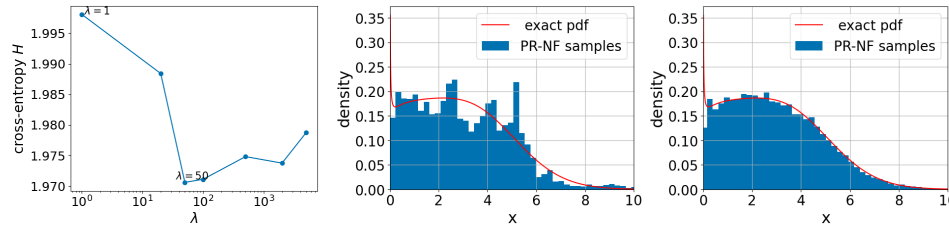


FIG. 3. The left panel shows the cross entropy $H(\lambda)$, which attains the minimum when $\lambda = 50$. The middle and right panels show the fitting performance for $\lambda = 1$ and $\lambda = 50$, respectively. It is observed that the accuracy of PR-NF model with $\lambda = 50$ is better than the case $\lambda = 1$. Without the tuning process of λ , the PR-NF model may fail to balance the \mathcal{L}_1 and \mathcal{L}_2 (e.g., $\lambda = 1$ case). The minimization of the cross entropy $H(\lambda)$ is an effective and correct approach to choose λ . The PR-NF model with an optimal parameter λ ($\lambda = 50$ case) achieves a good fitting performance.

We now use the well-trained PR-NF model ($\lambda = 50$) to sample X_t with variable initial distributions. The top row of Fig. 4 shows four different initial distributions, denoted as “ δ func”, “bar”, “sin2”, and “ricker”. The bottom row of Fig. 4 shows corresponding histogram of X_t generated by the PR-NF model, where a good agreement with the exact density is observed. The results demonstrate that the well-trained PR-NF model can handle different initial conditions without additional training process. Figure 5 shows the decay of the loss function of training dataset (left panel) and the decay of the Kullback–Leibler (KL) divergence of the four initial distributions (right panel). The KL divergence formula is defined as the relative entropy from the approximate density (generated from PR-NF) p_{approx} to the exact density p_{exact} , i.e.,

$$(5.4) \quad D_{\text{KL}}(p_{\text{exact}} \parallel p_{\text{approx}}) = \int_{-\infty}^{\infty} p_{\text{exact}}(x) \log\left(\frac{p_{\text{exact}}(x)}{p_{\text{approx}}(x)}\right) dx,$$

where D_{KL} can be approximated by the Riemann sum over a uniform mesh or the mean value of $\log\left(\frac{p_{\text{exact}}(x)}{p_{\text{approx}}(x)}\right)$ over the training dataset \mathcal{X} based on the exact solution in Eq. (5.2). We monitor the KL divergence for different distributions during the training process. The consistency of decays between loss function and KL divergence illustrates that the loss function \mathcal{L} defined in Eq. (3.5) involving the reversibility error is effective to be regarded as a loss function for normalizing flow.

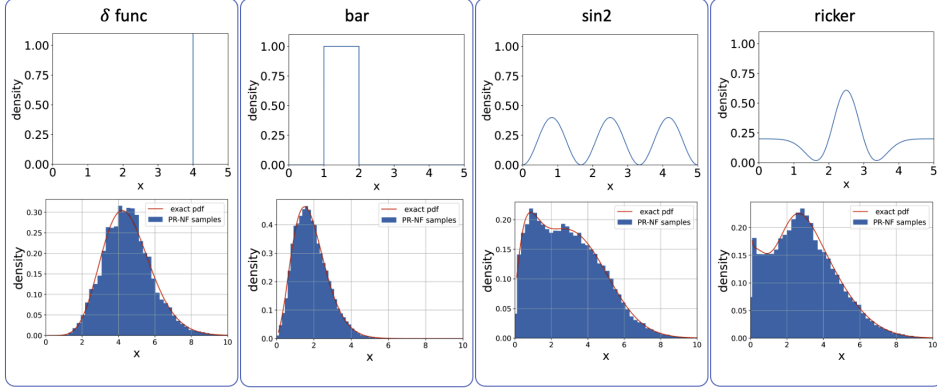


FIG. 4. The accuracy performance of the well-trained PR-NF model for test dataset. The top row shows the initial distributions of four dataset: δ func, bar, sin2, and ricker. The corresponding plots on the bottom row present the fitting between the exact density of X_t (red curve) and the histogram (generated by PR-NF model) at $t = 0.1$. The results demonstrate that the well-trained PR-NF model can handle various initial conditions without re-training.

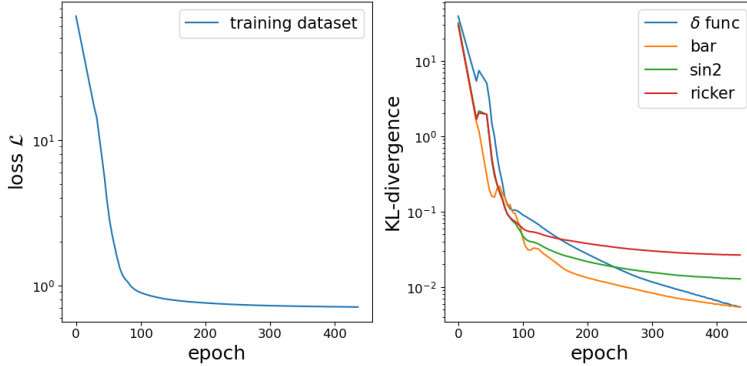


FIG. 5. The decay of loss function of training dataset (left panel) and the decay of KL divergence of four test dataset (right panel). We monitor the KL divergence during the training process. The consistency of decays between loss function and KL divergence demonstrates that the loss function \mathcal{L} defined in Eq. (3.5) involving the reversibility error is effective to be regarded as a loss function for normalizing flow.

To illustrate the application of our method to high-dimensional problems, consider the ten-dimensional SDE

$$(5.5) \quad X_t = X_0 + \int_0^t X_s ds + \int_0^t K X_s dW_s \quad \text{with } X_0 \in \mathcal{D},$$

how the proposed PR-NF method can be used to overcome some of these computational challenges in the case of magnetically confined high temperature plasmas in toroidal geometry. This configuration (known as tokamak) is the leading approach to achieve the elusive goal of controlled nuclear fusion for electricity production. The specific problem we consider is the simulation of relativistic runaway (RE) electrons produced during magnetic disruptions, see for example Ref. [2] and references therein. Understanding this problem is critical for the safe operation of nuclear fusion reactors.

The model of interest consists of the following set of SDEs

$$(5.7) \quad \begin{cases} dp = \left[E\xi - \frac{\gamma p}{\tau}(1 - \xi^2) - C_F(p) + \frac{1}{p^2} \frac{\partial}{\partial p} (p^2 C_A) \right] dt + \sqrt{2C_A} dW_p, \\ d\xi = \left[\frac{E(1 - \xi^2)}{p} + \frac{\xi(1 - \xi^2)}{\tau\gamma} - 2\xi \frac{C_B}{p^2} \right] dt + \frac{\sqrt{2C_B}}{p} \sqrt{1 - \xi^2} dW_\xi. \end{cases}$$

This two-dimensional reduced model tracks the evolution of the magnitude of the relativistic momentum, p , and $\xi = \cos \eta$, where η is the pitch angle between the particle velocity and the magnetic field which is assumed fixed and given. dW_p and dW_ξ are independent standard Brownian motions, E is the electric field, and τ the radiation damping time scale. The collision operator includes the momentum diffusion, C_A , pitch angle scattering, C_B , and Coulomb drag, C_F , which are defined as

$$\begin{aligned} C_A(p) &= \bar{v}_{ee} \bar{v}_T^2 \frac{\psi(y)}{y}, \quad C_F(p) = 2 \bar{v}_{ee} \bar{v}_T \psi(y), \\ C_B(p) &= \frac{1}{2} \bar{v}_{ee} \bar{v}_T^2 \frac{1}{y} \left[Z + \phi(y) - \psi(y) + \frac{y^2}{2} \delta^4 \right], \\ \phi(y) &= \frac{2}{\sqrt{\pi}} \int_0^y e^{-s^2} ds, \quad \psi(y) = \frac{1}{2y^2} \left[\phi(y) - y \frac{d\phi}{dy} \right], \quad y = \frac{1}{\bar{v}_T} \frac{p}{\gamma}, \\ \gamma &= \sqrt{1 + (\tilde{\delta} p)^2}, \quad \tilde{\delta} = \frac{\tilde{v}_T}{c} = \sqrt{\frac{2\tilde{T}}{mc^2}}, \quad \delta = \frac{\hat{v}_T}{c} = \sqrt{\frac{2\hat{T}_f}{mc^2}}, \quad \bar{v}_T = \sqrt{\frac{\hat{T}_f}{\tilde{T}}}, \\ \bar{v}_{ee} &= \left(\frac{\tilde{T}}{\hat{T}_f} \right)^{3/2} \frac{\ln \hat{\Lambda}}{\ln \tilde{\Lambda}}, \quad \ln \tilde{\Lambda} = 14.9 - \frac{1}{2} \ln 0.28 + \ln \tilde{T}, \quad \ln \hat{\Lambda} = 14.9 - \frac{1}{2} \ln 0.28 + \ln \hat{T}_f, \end{aligned}$$

with Z and c denoting the ion effective charge and the speed of light, respectively. Further details on this model can be found in Ref. [4, 25] and references therein.

We are interested in the hot-tail acceleration of electrons due to the rapid cooling of the plasma (thermal quench) during a magnetic disruption [23, 17]. We use a fast cooling model for the temperature and an electric field from Ohm's law with a Spitzer resistivity temperature dependent model $E = E_0 \left[\frac{\tilde{T}}{\hat{T}_f} \right]^{3/2}$, with typical model parameters $Z = 1$, $\tau = 6 \times 10^3$, $E_0 = 1/2000$, $\tilde{T} = 3$, $\hat{T}_f = 0.05$ and $mc^2 = 500$. The integration domain is $p \in (p_{\min}, p_{\max})$ and $\theta \in (0, \pi)$, where $(p_{\min}, p_{\max}) = (0.5, 5)$, and $t_{\max} = 26$. The different cases of initial conditions are obtained by sampling a family of Maxwellian distributions

$$(5.8) \quad f(p, \xi, t_0) = \frac{2p^2}{\pi^{1/2} p_0^3} e^{-(p/p_0)^2}, \quad \text{where } p_0 = \sqrt{\frac{\hat{T}_0}{\tilde{T}}},$$

normalized as $\int_0^1 \int_{-1}^1 \int_{p_{\min}}^{p_{\max}} f_0(p, \xi) dp d\xi = 1$, and parameterized by \hat{T}_0 . Exploration of the hot-tail generation of RE in this case requires the solution of this problem for different values of \hat{T}_0 . In the standard Monte Carlo approach this is a computational intense problem because each time \hat{T}_0 changes the problem needs to be recomputed for the new initial condition. However, as it will be shown bellow, this is not the case with the proposed PR-NF method.

In this problem the training dataset \mathcal{V} consists of $N_{\text{train}} = 30000$ samples with initial positions, $\{(p_0, \xi_0)^{(n)}\}$, $n = 1, \dots, N_{\text{train}}$, uniformly distributed in the integration domain and terminal positions, $(p_{t_{\max}}, \xi_{t_{\max}})^{(n)}$, obtained by a direct Monte Carlo simulation of Eqs. (5.7). The neural network architecture of the PR-NF model uses $N_{\text{hidden}} = 1$ hidden layer and $N_{\text{neuron}} = 512$ neurons. To choose the hyperparameter λ , which controls the relative importance of the pseudo-reversibility and the negative log-likelihood losses, we follow the same procedure as in Section 5.1. Namely, we select the value of λ for which the cross entropy, $H(\lambda)$, has a minimum, which in this case corresponds to $\lambda = 100$.

To check the accuracy of the PR-NF model we consider a test set of $N_{\text{test}} = 20000$ samples drawn from the Maxwellian distribution in Eq. (5.8) with $\hat{T}_0 = 10$. Fig. 7 compares the final probability density function (pdf) at $t_{\max} = 26$ computed with the PR-NF method and the direct Monte Carlo simulation. To construct the pdf from the N_{test} data points, we use a Gaussian kernel density estimation. The plots on the top row show the one-dimensional marginal pdfs for the pitch angle θ (left) and momentum p (right). The plots on the bottom row show the two-dimensional contour plots of the \log_{10} of the pdfs for the PR-NF (left) and the MC (right) simulations. The local pointwise differences between PR-NF and MC methods are of the order 10^{-2} , which implies a small error in the evaluation of quantities of interest like the production of runaway electrons shown in Fig. 8.

To illustrate the performance of the PR-NF method in the computation of the final state for different initial conditions, we consider the quantity of interest

$$(5.9) \quad n_{\text{RE}} = \int_{-1}^1 \int_{p^*}^{p_{\max}} f_{t_{\max}}(p, \xi) dp d\xi,$$

representing the total fraction of runaway electrons produced by the hot-tail mechanism during the thermal quench, where $f_{t_{\max}}$ is the density function of electrons at $t_{\max} = 26$, $p^* = 1.75$ is the RE energy threshold and p_{\max} is a numerical upper bound. We consider a family of Maxwellian initial conditions of the form in Eq. (5.8) with $\hat{T}_0 = 1, 2, 3, 4, 5, 6, 7, 8, 9, 10$. Figure 8 compares n_{RE} computed using a direct MC simulation that requires to solve the whole problem from the start for each value of \hat{T}_0 , with the PR-NF method that reduces the computation to the direct evaluation of the final state using the trained neural network. This numerical simulation is based on $N_{\text{sample}} = 20000$ samples for different \hat{T}_0 . By using a single PR-NF model, we can obtain the orbits of particles for ten initial conditions without any additional simulations or training. However, the Monte Carlo method has to repeatedly simulate the particles' orbits for ten times. For the simulation, the time step size of the MC method is $\Delta t = 0.001$ and the number of epochs of the PR-NF method is $N_{\text{epoch}} = 20000$. We record the running wall-clock time (measured using the python function "time.time()") between these two methods. For the results in Fig. 8, the error between the PR-NF and MC method (viewed as the ground-truth) is acceptable. The accuracy of PR-NF model is enough to predict and analyze the profile of fraction runaway electrons production rate n_{RE} . Moreover, the total running time of

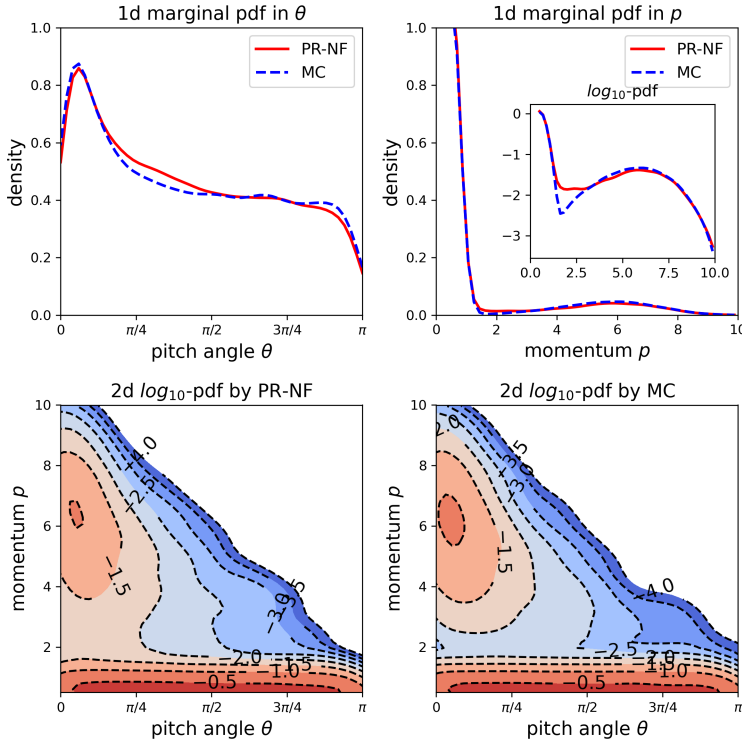


FIG. 7. Final state of runaway electrons probability density function, $f(\theta, p, t_{max})$, according to the model in Eq. (5.7) with initial condition, $f(\theta, p, t_0)$ in Eq. (5.8) with $T_0 = 10$. The top row compares the 1d marginal distributions for the pitch angle (left) and the momentum (right) computed using the PR-NF and the MC methods. The inset in the the top plot on the right highlights, in logarithmic scale, the bump in the distribution resulting from the acceleration of the hot tail. The contour plots at the bottom compare the 2d distributions using a \log_{10} scale. The local pointwise differences between PR-NF and MC methods are of the order 10^{-2} . Such agreement between MC and the PRNF methods is sufficient to ensure the accuracy of quantity of interest, for example, the runaway electron production rate in Fig. 8.

the MC method of these ten cases of Maxwellian distribution is around $C_{MC} = 4000$ sec. The total running time of the PR-NF method consists of two parts, the offline cost is around $C_{offline} = 1354$ sec and the online cost is around $C_{online} = 12$ sec. The PR-NF model is faster than the MC method, especially on the online cost. This efficiency advantage is more valuable when we handle a large number of Maxwellian distributions.

5.3. Passive scalar advection-diffusion transport in a 3D chaotic flow.

Understanding passive scalar transport is a problem of significant interest in fluid dynamics in general and environmental engineering, oceanography, and atmospheric sciences in particular. By passive we mean that the transported scalar exactly follows the given velocity field without modifying it.

As a specific example to illustrate the application of the PR-NF method to this problem, we consider the ABC (Arnold-Beltrami-Childress) flow [6] which is a three-dimensional incompressible velocity field which is an exact solution of Euler's equation. In Cartesian coordinates this velocity field has components $\mathbf{v} = (v_x, v_y, v_z)$ with $v_x = A \sin z + C \cos y$, $v_y = B \sin x + A \cos z$ and $v_z = C \sin y + B \cos x$. For a wide range

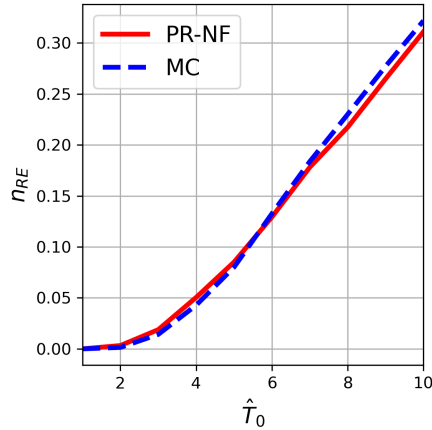


FIG. 8. Quantity of interest n_{RE} in Eq. (5.9) represents the production of runaway electrons as function of the parameter \hat{T}_0 in Eq. (5.8). The red curve shows the result using the PR-NF surrogate model and the blue curve the result using the direct MC method. A single PR-NF model can compute n_{RE} for ten initial conditions without any additional simulations or training, where the online cost is much cheaper than MC method. The accuracy of PR-NF model is sufficient to predict the profile of the production rate n_{RE} as the MC method (around 1% absolute error is acceptable here).

of the A , B and C parameters, this flow is not integrable. That is, it exhibits chaotic advection and the sensitive dependence on initial condition gives rise to rapid mixing and long-range transport [21].

In addition to advection, passive scalar transport is affected by diffusion. In particle based simulations this important effect can be modeled by adding a stochastic term. Following this approach we consider the following set of SDEs

$$(5.10) \quad \begin{cases} dx = P_e [A \sin z + C \cos y] dt + dW_x, \\ dy = P_e [B \sin x + A \cos z] dt + dW_y, \\ dz = P_e [C \sin y + B \cos x] dt + dW_z. \end{cases}$$

where dW_x , dW_y and dW_z are independent Brownian motions, and the Peculé number, P_e is a dimensionless parameter controlling the relative importance of advection and diffusion. When, $P_e \ll 1$, transport is dominated by diffusion and when, $P_e \gg 1$, transport is dominated by advection.

The initial conditions, $\{x_0^{(n)}, y_0^{(n)}, z_0^{(n)}\}_{n=1}^{N_{\text{train}}}$, of the training dataset consists of an ensemble of $N_{\text{train}} = 30000$ random points uniformly distributed in the cubic domain $\mathcal{D} = [0, 2\pi] \times [0, 2\pi] \times [0, 2\pi]$. The terminal positions, $\{x_{t_{\text{max}}}^{(n)}, y_{t_{\text{max}}}^{(n)}, z_{t_{\text{max}}}^{(n)}\}_{n=1}^{N_{\text{train}}}$, of the training dataset are obtained by a direct Monte Carlo simulation of Eq. (5.10). In the calculation presented we use $t_{\text{max}} = 2$, and model parameters $P_e = 3$, $A = 1$, $B = 1$, and $C = 0.25$. For the PR-NF neural network model we use $N_{\text{hidden}} = 1$ hidden layer with $N_{\text{neuron}} = 512$ neurons. Once the training process is done, the PR-NF model can be used as a surrogate model to predict the final state for various initial conditions, without the need to integrate Eqs. (5.10).

As a first test, we apply the PR-NF to predict the final state of an initial condition

of the form

$$(5.11) \quad f(x, y, z, t_0) = H(x, y, z) \exp \left[- \left(\frac{x - x_c}{\sigma_x} \right)^2 - \left(\frac{y - y_c}{\sigma_y} \right)^2 - \left(\frac{z - z_c}{\sigma_z} \right)^2 \right],$$

modeling, for example, a Gaussian-shaped cloud of a pollutant, with $\sigma_x = \pi/3$, $\sigma_y = \pi/5$, $\sigma_z = \pi/4$, localized at $(x_c, y_c, z_c) \in \mathcal{D}$, where $H(x, y, z) = 1$ if $(x, y, z) \in \mathcal{D}$ and $H(x, y, z) = 0$ otherwise. Figure 9 shows a good agreement between the final pdf of the passive scalar, $f(x, y, z, t_{\max})$, computed with the PR-NF surrogate model and the pdf computed using direct Monte Carlo simulation for the case $(x_c, y_c, z_c) = (\pi/2, \pi, \pi)$. Since both methods are particle-based, once the discrete particle data have been obtained, the corresponding pdfs are constructed using a standard Gaussian-kernel estimation. To ease the comparison of these 3d pdfs, Fig. 9 shows the 1d marginal distributions, e.g., $g(x) = \int dy \int dz f(x, y, z, t_{\max})$, and the 2d marginal distributions, e.g., $g(x, y) = \int dz f(x, y, z, t_{\max})$. The mixing due to the combination of chaotic advection and diffusion rapidly displaces the scalar outside the \mathcal{D} domain.

As a second application we consider a ‘‘target’’ transport problem of interest, for example, to environmental fluid dynamics. The problem consists of finding the concentration of the scalar in a target domain, $\mathcal{T} = [x_{\min}, x_{\max}] \times [-\infty, \infty] \times [z_{\min}, z_{\max}]$, resulting from the transport of a concentrated pollutant cloud released inside the $\mathcal{D} = [0, 2\pi] \times [0, 2\pi] \times [0, 2\pi]$ domain. The initial cloud will be described using the Gaussian model in Eq. (5.11) with $\sigma_x = \pi/3$, $\sigma_y = \pi/5$, $\sigma_z = \pi/4$. The y -coordinate of the cloud will be fixed at $y_c = \pi$ and the goal is to compute the total scalar density in \mathcal{T} as function of the (x_c, z_c) coordinates of the center of the initial cloud in \mathcal{D} . The quantity of interest in this case is

$$(5.12) \quad n_{\mathcal{T}}(x_c, z_c) = \int_{x_{\min}}^{x_{\max}} \int_{-\infty}^{\infty} \int_{z_{\min}}^{z_{\max}} f(x, y, z, t_{\max}) dx dy dz,$$

and for the calculation presented here we will use $x_{\min} = 0$, $x_{\max} = \pi$, $z_{\min} = 2\pi$, and $z_{\max} = 3\pi$.

To perform this calculation a $N_x \times N_z$ uniform grid is constructed in the $(x_c, z_c) \in [0, 2\pi] \times [0, 2\pi]$ space and the $N_x N_z = N_{\text{ic}}$ grid nodes are used to define the ensemble $\{x_c^i, z_c^i\}_{i=1}^{N_{\text{ic}}}$. For each element of the ensemble, the standard direct Monte Carlo approach requires the solution of the system of SDE in Eq. (5.10) for N_{test} particles with initial conditions sampled from the Gaussian cloud in Eq. (5.11) centered at $(x_c^i, y_c = \pi, z_c^i)$. In total, this approach requires $N_{\text{ic}} N_{\text{test}}$ solutions of the SDEs. On the other hand, the PR-NF method only requires to solve the SDE in Eq. (5.10) for N_{train} initial conditions and, once the training is done, the computation of the $N_{\text{ic}} N_{\text{test}}$ initial conditions can be done by simply evaluating the surrogate neural network model.

In the case discussed here we use $N_x = N_z = 21$, and $N_{\text{test}} = 20000$. With the Monte Carlo method this requires solving 8.82×10^6 SDEs. For $t_{\text{final}} = 2$, with step size $\Delta t = 0.001$, the total run-time to produce the results reported in Fig. 10 was $C_{\text{MC}} = 5320$ sec. On the other hand, the training of the PR-NF neural network, like in the previous calculation, is done using $N_{\text{train}} = 30000$, $N_{\text{hidden}} = 1$ hidden layer with $N_{\text{neuron}} = 512$ neurons, and $N_{\text{epoch}} = 20000$. For these parameters, the offline cost of the training is around $C_{\text{offline}} = 2200$ sec. But, once the training is done, the evaluation of the different initial conditions has minimal cost. In particular, the total PR-NF run-time to produce the results reported in Fig. 10 is of the order $C_{\text{online}} = 50$ sec. The contour plots of $n_{\mathcal{T}}$ shown in Fig. 10 provided evidence that the much more

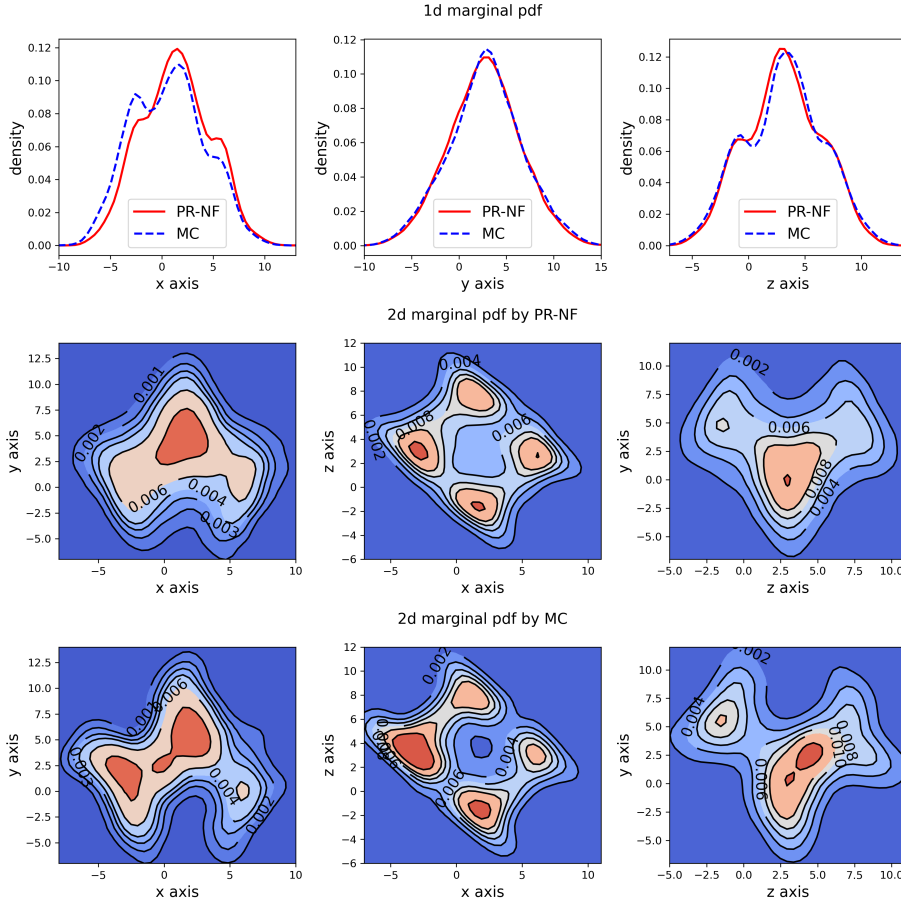


FIG. 9. Final state of the probability density function, $f(x, y, z, t_{max})$, of the scalar resulting from the advection-diffusion in the ABC fluid velocity model with diffusion in Eq. (5.10) for the initial condition, $f(x, y, z, t_0)$, in Eq. (5.11). Since the pdf is 3d, to ease the comparison between the PR-NF and the MC methods, we show the 1d marginal distributions in the top row and the 2d marginal distribution if the bottom rows. The contour plots in one column share the same level, and the scale is of the order 10^{-3} . The agreement between the two methods is sufficient to ensure the accuracy of the quantity of interest shown in Fig. 10.

efficient PR-NF surrogate model reproduces well the results obtained with the direct, time-consuming, MC method for the target transport problem.

6. Conclusion. We proposed an accurate and efficient normalizing-flow algorithm for the solution of stochastic differential equations with arbitrary initial conditions. Our approach leverages the pseudo-reversible normalizing flow neural network framework. The novelty of our normalizing flow approach can be viewed from two perspectives. Firstly, it enables learning the distribution of the final state based on any given initial state. This allows the model to be trained just once, and then applied to handle various initial distributions effectively. Secondly, we develop a pseudo-reversible neural network architecture that relaxes the strict reversibility constraint. This feature simplifies the implementation of feed-forward neural networks, which model both forward and inverse flows.

Our subsequent objective is to expand the applicability of the proposed method to

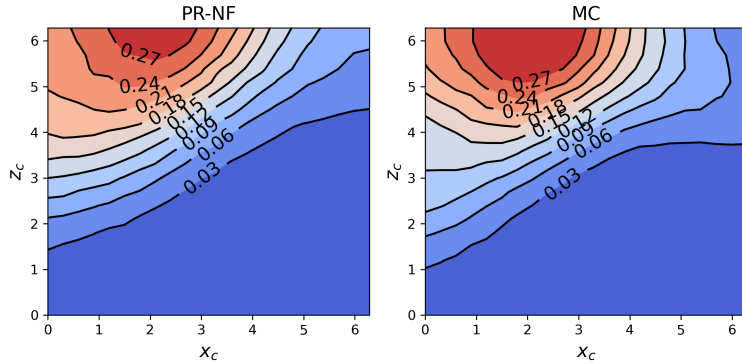


FIG. 10. Contour plots of quantity of interest $n_\tau(x_c, z_c)$ in Eq. (5.12) computed using the PR-NF surrogate model (left panel) and the direct MC method (right panel). For a given (x_c, z_c) , $n_\tau(x_c, z_c)$ denotes the total density of the scalar in the target region $\mathcal{T}(x, y, z) = [0, \pi] \times [-\infty, \infty] \times [2\pi, 3\pi]$ resulting from the transport of an initial Gaussian cloud, Eq. (5.11), centered at $(x_c, y_c = \pi, z_c) \in \mathcal{D}(x, y, z) = [0, 2\pi] \times [0, 2\pi] \times [0, 2\pi]$. The agreement of the two calculation provides evidence of the accuracy of the significantly faster PR-NF method (absolute error between two methods in n_τ is of the order 10^{-2}). The results of PR-NF (left panel) is sufficient to simulate the profile of n_τ . Moreover, the online cost of PR-NF method is about 100 times faster than MC method.

tackle more complex problems. For example, the two-dimensional runaway electron model discussed in Section 5.2 is a reduced 2-D plasma transport model. Going beyond this simplified description, we envision extending the capabilities of the PR-NF model to encompass the six-dimensional full-orbit transport model, which poses significant challenges when employing PDE-based methods. Additionally, we aim to explore the complete dynamics of stochastic differential equations, not limited to a single time instant.

Acknowledgement. This material is based upon work supported by the U.S. Department of Energy, Office of Science, Office of Advanced Scientific Computing Research, Applied Mathematics program under the contract ERKJ387, Office of Fusion Energy Science, and Scientific Discovery through Advanced Computing (SciDAC) program, at the Oak Ridge National Laboratory, which is operated by UT-Battelle, LLC, for the U.S. Department of Energy under Contract DE-AC05-00OR22725.

REFERENCES

- [1] G.-J. BOTH AND R. KUSTERS, *Temporal normalizing flows*, arXiv preprint arXiv:1912.09092, (2019).
- [2] B. N. BREIZMAN, P. ALEYNIKOV, E. M. HOLLMANN, AND M. LEHNEN, *Physics of runaway electrons in tokamaks*, Nuclear Fusion, 59 (2019), p. 083001.
- [3] A. CRESWELL, T. WHITE, V. DUMOULIN, K. ARULKUMARAN, B. SENGUPTA, AND A. A. BHARATH, *Generative adversarial networks: An overview*, IEEE signal processing magazine, 35 (2018), pp. 53–65.
- [4] D. DEL-CASTILLO-NEGRETE, M. YANG, M. BEIDLER, AND G. ZHANG, *Generation and mitigation of runaway electrons: spatio-temporal effects in dynamic scenarios*, tech. report, Oak Ridge National Lab.(ORNL), Oak Ridge, TN (United States), 2021.
- [5] L. DINH, J. SOHL-DICKSTEIN, AND S. BENGIO, *Density estimation using real nvp*, arXiv preprint arXiv:1605.08803, (2016).
- [6] T. DOMBRE, U. FRISCH, J. M. GREENE, M. HÉNON, A. MEHR, AND A. M. SOWARD, *Chaotic streamlines in the abc flows*, Journal of Fluid Mechanics, 167 (1986), pp. 353–391.
- [7] L. FENG, XIAODONG ZENG AND T. ZHOU, *Solving time dependent fokker-planck equations via temporal normalizing flow*, Communications in Computational Physics, 32 (2022), pp. 401–

- 423.
- [8] W. GRATHWOHL, R. T. CHEN, J. BETTENCOURT, I. SUTSKEVER, AND D. DUVENAUD, *Fjord: Free-form continuous dynamics for scalable reversible generative models*, arXiv preprint arXiv:1810.01367, (2018).
 - [9] L. GUO, H. WU, AND T. ZHOU, *Normalizing field flows: Solving forward and inverse stochastic differential equations using physics-informed flow models*, Journal of Computational Physics, 461 (2022), p. 111202.
 - [10] T. A. KELLER, J. W. PETERS, P. JAINI, E. HOOGEBOOM, P. FORRÉ, AND M. WELLING, *Self-normalizing flows*, in International Conference on Machine Learning, PMLR, 2021, pp. 5378–5387.
 - [11] D. P. KINGMA AND J. BA, *Adam: A method for stochastic optimization*, arXiv preprint arXiv:1412.6980, (2014).
 - [12] I. KOBYZEV, S. J. PRINCE, AND M. A. BRUBAKER, *Normalizing flows: An introduction and review of current methods*, IEEE transactions on pattern analysis and machine intelligence, 43 (2020), pp. 3964–3979.
 - [13] Y. LU, R. MAULIK, T. GAO, F. DIETRICH, I. G. KEVREKIDIS, AND J. DUAN, *Learning the temporal evolution of multivariate densities via normalizing flows*, Chaos: An Interdisciplinary Journal of Nonlinear Science, 32 (2022), p. 033121.
 - [14] B. ØKSENDAL AND B. ØKSENDAL, *Stochastic differential equations*, Springer, 2003.
 - [15] G. PAPAMAKARIOS, E. NALISNICK, D. J. REZENDE, S. MOHAMED, AND B. LAKSHMINARAYANAN, *Normalizing flows for probabilistic modeling and inference*, The Journal of Machine Learning Research, 22 (2021), pp. 2617–2680.
 - [16] G. PAPAMAKARIOS, T. PAVLAKOU, AND I. MURRAY, *Masked autoregressive flow for density estimation*, Advances in neural information processing systems, 30 (2017).
 - [17] Y. V. PETROV, P. PARKS, AND R. HARVEY, *Numerical simulation of the hot-tail runaway electron production mechanism using cql3d and comparison with smith-verwichte analytical model*, Plasma Physics and Controlled Fusion, 63 (2021), p. 035026.
 - [18] A. PINKUS, *Approximation theory of the mlp model in neural networks*, Acta numerica, 8 (1999), pp. 143–195.
 - [19] D. REZENDE AND S. MOHAMED, *Variational inference with normalizing flows*, in International conference on machine learning, PMLR, 2015, pp. 1530–1538.
 - [20] O. RIPPEL AND R. P. ADAMS, *High-dimensional probability estimation with deep density models*, arXiv preprint arXiv:1302.5125, (2013).
 - [21] M. F. SHLESINGER, G. M. ZASLAVSKY, AND J. KLAFTER, *Strange kinetics*, Nature, 363 (1993), pp. 31–37.
 - [22] R. W. SHONKWILER AND F. MENDIVIL, *Explorations in monte carlo methods*, Springer Science & Business Media, 2009.
 - [23] A. STAHL, O. EMBRÉUS, G. PAPP, M. LANDREMAN, AND T. FÜLÖP, *Kinetic modelling of runaway electrons in dynamic scenarios*, Nuclear Fusion, 56 (2016), p. 112009.
 - [24] Y. TENG, Z. WANG, L. JU, A. GRUBER, AND G. ZHANG, *Level set learning with pseudo-reversible neural networks for nonlinear dimension reduction in function approximation*, arXiv preprint arXiv:2112.01438, (2021).
 - [25] M. YANG, G. ZHANG, D. DEL CASTILLO-NEGRETE, AND M. STOYANOV, *A feynman-kac based numerical method for the exit time probability of a class of transport problems*, Journal of Computational Physics, 444 (2021), p. 110564.